Steady-state liquid sloshing in a rectangular tank with a slat-type screen in the middle: Quasilinear modal analysis and experiments

O. M. Faltinsen,[a] R. Firoozkoohi, and A. N. Timokha
Centre for Ships and Ocean Structures and Department of Marine Technology, Norwegian University of Science and Technology, NO-7091 Trondheim, Norway

Two-dimensional resonant liquid sloshing in a rectangular tank equipped with a central slat-type screen is studied theoretically and experimentally with focus on *nonsmall* solidity ratios of the screen ($0.5 \lesssim \mathrm{Sn} \lesssim 0.95$), nonlarge number of slots ($N \lesssim 50$), and steady-state conditions. The tank is horizontally and harmonically excited with frequencies in a range covering the two lowest primary-excited natural sloshing resonance frequencies in the corresponding clean tank. The liquid depth is finite. Theoretical analysis is based on the multimodal method with linear free-surface conditions and a quadratic pressure drop condition at the screen expressing an "integral" effect of the screen-induced cross-flow separation (or jet flow). New experimental data on the maximum wave elevations at the wall are compared with the theoretical predictions. Very good agreement is shown for the smallest forcing amplitudes (the forcing amplitude-to-tank width ratio is ≈ 0.001). Increasing the nondimensional forcing amplitude to ≈ 0.01 leads to discrepancies due to secondary resonance causing the energy context from the two primary-excited antisymmetric modes to other, first of all, symmetric modes. A further increase of the nondimensional forcing amplitude to 0.03 leads to more complex secondary resonance effects. Specific surface wave phenomena, e.g., wave breaking, are experimentally observed and documented by photographs and videos.
© *2011 American Institute of Physics*. [doi:10.1063/1.3562310]

I. INTRODUCTION

Rectangular tanks with screens are used for antirolling tanks of ships and tuned liquid dampers (TLDs) of tall buildings. Properly tuned sloshing is an efficient tool for suppressing oscillations of the carrying structure. For these applications, a design requirement is that the lowest resonant sloshing frequency should almost not be affected by screens, i.e., it must remain almost the same as for the clean tank and relatively close to the most important structural natural frequency and the roll natural frequency. A rough guideline is then that the screen *solidity ratio* Sn, i.e., the ratio of the area of the shadow projected by the screen on a plane parallel to the screen to the total area contained within the frame of the screen is relatively small, $\mathrm{Sn} \lesssim 0.5$. The free-surface nonlinearity may be important.[1] This especially matters for antirolling and ship tanks when the nondimensional tank motion magnitudes (scaled by the cross-dimensional tank length l) are clearly larger than for TLDs.

The cargo ship liquid tanks with swash bulkheads is another application dealing with sloshing in rectangular tanks. A swash bulkhead is a bulkhead with holes and has from a hydrodynamic point of view similarities with a screen. The objectives are to provide sloshing damping as well as to *change the lowest resonance frequency* to a higher frequency range where the wave-induced ship velocity and acceleration are less severe. The consequence is that, in contrast to TLDs, slotted swash bulkheads are characterized by a higher solidity ratio, e.g., $\mathrm{Sn} \approx 0.9$. The optimum solidity ratio is not the

highest value $\mathrm{Sn}=1$ which means that the screen becomes a solid wall dividing the liquid domain into independent compartments. Similar devices as swash bulkheads are, for instance, used in fuel tanks of rockets and oil-gas separators on floating platforms.

Bearing in mind the swash bulkheads in rectangular ship tanks, we focus in the present paper on the *steady-state* two-dimensional liquid sloshing in a rectangular tank with a central slat-type screen and the specific geometric and physical parameters which are, in contrast to earlier TLDs studies, characterized by

- $0.5 \lesssim \mathrm{Sn} \lesssim 0.95$;
- a limited number of openings (slots, gaps) in the screen ($N \lesssim 50$);
- finite liquid depths;
- a wider forcing frequency range covering not only the lowest natural sloshing frequency for the corresponding clean tank, σ_1^*, but also the next primary excited natural sloshing frequency σ_3^*.

The latter frequency range is needed because, in contrast to a TLD with lower solidity ratios, frequencies corresponding to the resonant sloshing responses with $0.5 \lesssim \mathrm{Sn} \lesssim 0.95$ are expected to be away from those for the corresponding clean tank. The lateral excitations are considered. A particular goal is to understand the physics of liquid sloshing dynamics versus the input parameters, the solidity ratio Sn, the forcing frequency σ, and the forcing amplitude η_{2a} with emphasis on the resonance frequencies as a function of Sn. Understanding the role of the free-surface nonlinearity is an-

---
[a]Electronic mail: odd.faltinsen@ntnu.no.

other particular goal. Three different nondimensional amplitudes, $\eta_{2a}/l = 0.001$, 0.02, and 0.03 were tested in the experiments.

To the best of the authors' knowledge, the literature on the liquid sloshing dynamics in tanks with screens of solidity ratio higher than 0.5 is rare. Typical examples in the papers by Kaneko and Ishikawa,[2] Tait *et al.*,[3] Love and Tait,[1] and Warnitchai and Pinkaew[4] are associated with TLDs and Sn $\lesssim 0.5$. They extensively employ the fact that the natural sloshing frequencies and modes remain *almost the same* as for the corresponding clean tank (without screen). The focus is mainly on the resonance response with the forcing frequencies close to the first natural frequency of the corresponding clean tank, σ_1^*. For analyzing this resonance, Kaneko and Ishikawa,[2] Tait *et al.*,[3] and Love and Tait[1] use different linear and nonlinear modal methods in which the corresponding modal equations are derived (Love and Tait[1] takes the nonlinear modal system by Faltinsen and Timokha[5]) based on the natural sloshing modes of the corresponding clean tank. These modal solutions make it possible to estimate the pressure field at the screen and, using the pressure drop condition, derive quadratic damping term in the corresponding modal equations. The pressure drop condition appears as a generalization of the viscous drag term in Morison's equation. This condition requires empirical information on the so-called pressure drop coefficient which, for instance, is well-known for an orifice meter device and the modeling of the screen effect in air ventilation systems. Reviews on usage of this condition can be found in Refs. 6 and 7. Additional examples of using this condition for liquid sloshing dynamics and external surface wave problems can be found in the papers by Molin[8] and Faltinsen *et al.*[9]

When Sn $\rightarrow 1$, the screen becomes a rigid wall. The modal solution employing the natural sloshing modes of the corresponding clean tank used in the aforementioned TLD analysis is then not more applicable. The resonant peaks are then expected not at σ_{2i-1}^* (odd natural sloshing frequencies of the clean tank). This fact was first documented in the famous NASA Report[10] for a circular sectored tank. An attempt to describe the general *trend* in changing the *resonant* sloshing frequencies with increasing Sn in a rectangular tank with two-dimensional flows is given in Sec. 6.8 of Ref. 11. The screen was installed in the middle of the rectangular tank. Linear sloshing theory was employed. The idea was to consider the modal solutions in the two screen-separated compartments and, thereafter, match these solutions at the screen by using continuity of the mean flux velocity and the averaged pressure drop condition which should play the role of transmission boundary conditions. An extension of this approach was done by Faltinsen *et al.*[9] Realizing this idea showed success in describing (i) the resonance response amplitude for σ close to σ_1^* (the first natural frequency for the corresponding clean tank), and (ii) the general qualitative fact of disappearance of the resonance peaks at σ_1^* and σ_3^* and appearance of the resonance peak at σ_2^* (which is the lowest natural sloshing frequency for the compartments) as Sn $\rightarrow 1$. Due to quadratic nature of the pressure drop condition, the results on the resonance peaks depend on the forcing amplitude. Furthermore, working on Ref. 9, we found out

that this approach is not precise in identification of the resonance peak positions as the forcing amplitude becomes smaller and Sn tends to 1. Even though the experimental forcing amplitude was sufficiently small (the forcing amplitude-to-tank width is about 0.001), this theoretical approach gave wrong resonance peak position in a frequency range about σ_3^*. Explanation comes from the fully linear analysis by Faltinsen and Timokha[12] who study the *linear* natural sloshing frequencies and modes neglecting flow separation (jet flow) at the slotted screen in the spirit of earlier papers on either surface-piercing barriers[13] or baffles.[14] Faltinsen and Timokha[12] showed in their linear analysis that, when Sn $\lesssim 0.5$, the screen-corrected natural sloshing frequencies remain almost the same as for the corresponding clean tank (consistent with earlier TLD analysis), but, when Sn increases in the range $0.5 \lesssim$ Sn < 1, the first natural sloshing frequency σ_1 (and the corresponding mode) in the screen-equipped tanks continuously vanishes, $\sigma_1 \rightarrow 0$, but the third one, $\sigma_3 \rightarrow \sigma_2^*$, as Sn $\rightarrow 1$. Because Faltinsen and Timokha[12] do *not* use the nonlinear pressure drop condition, this result on the natural sloshing frequencies and modes is independent of the forcing amplitude, i.e., it is the limit case on the resonance frequencies when the forcing amplitude tends to zero. The change of the theoretical natural frequencies by this linear theory is quantitatively consistent with experiments conducted with their smallest forcing amplitude $\eta_{2a}/l \approx 0.001$.

The transformations of the natural sloshing modes and frequencies within the linear approximation by Faltinsen and Timokha[12] are an important factor which should be accounted for in description of the forced resonant liquid sloshing and accurate identification of the resonance sloshing frequencies for $0.5 \lesssim$ Sn < 1. As we will show in the present paper, accounting for both these transformations and the pressure drop at the screen makes the multimodal technique much more complicated. The transformations are, however, not important for TLDs, thus, when $0 <$ Sn $\lesssim 0.5$, the interested reader can use, e.g., the modal theories Kaneko & Ishikawa,[2] Tait *et al.*,[3] and Love and Tait,[1] instead of following the present analysis.

The experimental setup, measured wave elevations at the walls, and video observations are reported in Secs. III and IV. The latter section includes also comparison with quasilinear multimodal theory constructed in Sec. II. The quasilinear multimodal theory is constructed based on the natural sloshing modes by Faltinsen and Timokha[12] and the well-known linear multimodal method whose description is given, e.g., in Chap. 5 of Ref. 11. A novelty is that we also account for the pressure drop condition by selecting the approach-velocity component from the singular (at the sharp slot edges) natural sloshing modes by Faltinsen and Timokha.[12] The quasilinear theory accounts therefore for the change of the natural sloshing modes (frequencies) versus the screen geometry as well as an "integral" effect of the local flow separation (or jet flow) by means of the pressure drop condition. However, this theory neglects the free-surface nonlinearity. Adopting the pressure drop condition implicitly assumes that the liquid motions in the whole tank are generally well described by the potential incompressible inviscid hydrodynamic model and that flow separation (or jet flow) at

the screen is only localized in a relatively small neighborhood of the screen.

Even though we postulate the linearized free-surface conditions, the nonlinear pressure drop condition introduces the $(\cdot|\cdot|)$-type quadratic quantities in terms of the generalized velocities in the corresponding modal equations. For TLD-related applications with resonant excitation at the lowest natural frequency, one can, e.g., follow Tait *et al.*[3] to get simpler expressions depending only on the dominant modes. These quantities can then be interpreted as quadratic damping terms causing finite resonant response at σ_1^* (see a review on the quadratic damping for linear oscillators in Ref. [15]). An alternative approach is to use a Morison-equation formulation instead of the pressure drop condition at the screen with $0 < \mathrm{Sn} \lesssim 0.5$ (see Sec. 6.7 of Ref. [11]). The latter approach provided very satisfactory agreement with experiments by Warnitchai and Pinkaew.[4] In the present paper, the hydrodynamic coefficients of the modal equations, including the natural frequencies σ_i, change with Sn, the number and position of the slots. The quadratic terms should then include all the generalized coordinates and, along with damping, cause an energy redistribution between different screen-modified natural sloshing modes.

Agreement between the quasilinear theory and experiments is almost ideal for the smallest forcing amplitude-to-tank width ratio equal to 0.001 (the liquid depth-to-the tank width ratio is 0.4). The results are reported in Sec. IV A. Discrepancies for the lowest and largest tested Sn, Sn $=0.4725$ and 0.95125, are explained by the free-surface nonlinearity causing a soft-spring type response behavior similar as for theoretical steady-state sloshing in clean rectangular tanks with a finite depth (see, e.g., Chap. 8 in Ref. [11]). Increasing the nondimensional forcing amplitude to 0.01 (Sec. IV B) leads to a series of new experimentally observed free-surface phenomena. The paper presents the corresponding photographs and videos. Implicitly, these free-surface phenomena, e.g., wave breaking, runup with jets at the walls, indicate importance of the free-surface nonlinearities. The observed free-surface phenomena are mainly documented in the frequency range covering σ_2^* and σ_3^*. The latter is explained by the fact that resonance at $\sigma \approx \sigma_1^*$ leads to a larger cross-flow at the screen, and, therefore, causes a larger damping due to flow separation (or jet flow). The experimental response curves are characterized by extra resonance peaks in this frequency range. The modal analysis shows that these peaks are a consequence of the secondary resonance due to the second-order free-surface nonlinearity. According to Faltinsen and Timokha,[5] this kind of the secondary resonance amplifies symmetric natural sloshing modes which are not directly excited by the horizontal tank forcing. Theoretical description of the secondary resonance may require the so-called adaptive nonlinear multimodal modeling elaborated by Faltinsen and Timokha[5] for the clean rectangular tank. However, the quasilinear theory describes the general trend in changing the main resonance peak position.

In Sec. IV C, we present experimental data for the largest tested forcing amplitude, $\eta_{2a}/l=0.03$, which were conducted with the liquid depth-to-the tank width, $h/l=0.35$. The experimental observations show very steep waves with
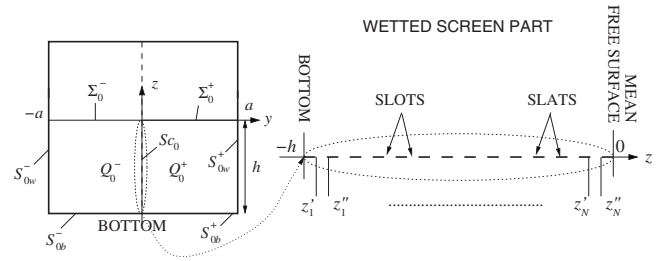

FIG. 1. The rectangular tank with a slat-type screen in the middle. Basic geometric notations.

strong wave breaking, runup as well as overturning and formation of gas pockets. Implicitly, this indicates amplifications of the higher natural modes via the free-surface nonlinearity mechanism. The quasilinear theory shows qualitatively how the resonance frequencies change with Sn, but cannot be used to quantify the steady-state wave amplitude response. Further, the experiments detect the multiple resonance peaks for $0.5 \lesssim \mathrm{Sn} \lesssim 0.9$ as well as the multibranching of the corresponding experimental response curves. In contrast to the case with $\eta_{2a}/l=0.01$, this cannot be easily explained by the secondary resonance phenomena due to the second-order nonlinearity. A dedicated study is required.

II. QUASILINEAR MULTIMODAL THEORY

A. Preliminaries

1. Basic notations and limit cases

Two-dimensional liquid sloshing is considered in a rectangular tank of width $l=2a$ with a slat-type screen installed at the tank middle as shown in Fig. 1. The figure introduces geometric notations and the body-fixed coordinate system. The rectangular tank is forced horizontally with displacements $\eta_2(t)$. The screen appears as a thin solid plate with a series of perforated horizontal slots. The screen thickness is neglected. In the linear free-surface analysis, we consider only the mean wetted screen part Sc_0 and assume that it has N submerged slots. When the set So_0 denotes all the wetted rigid slats, and Op_0 is the total set of submerged slots ($\mathrm{Sc}_0 = \mathrm{Op}_0 \cup \mathrm{So}_0$), this numerical sequence defines them as follows:

$$\mathrm{So}_0 = \{(0,z) : -h \le z \le z_1', \ z_1'' \le z \le z_2', \dots, \ z_N'' \le z \le 0\},$$

$$\mathrm{Op}_0 = \{(0,z) : -h \le z_1' < z < z_1'', \dots, \ z_N' < z < z_N'' \le 0\},$$

$$(1)$$

where h is the liquid depth. Based on definition (1), we can introduce the solidity ratio of the mean wetted screen part as follows:

$$\mathrm{Sn} = \frac{h - \Sigma_{j=1}^{N}(z_j'' - z_j')}{h}. \tag{2}$$

As we see, the solidity ratio is a function of h.

An inviscid and incompressible liquid with irrotational flow is assumed everywhere in the mean liquid domain $Q_0 = Q_0^- \cup Q_0^+$ *except* in a small neighborhood of the screen Sc_0. The *linear sloshing* theory is adopted, namely, the wave slope is assumed asymptotically small (see Chap. 5 in Ref.
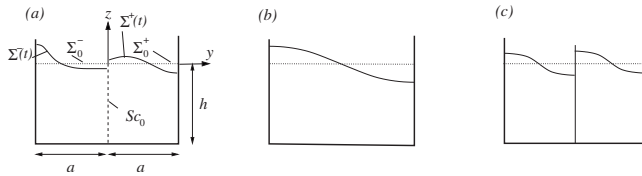
FIG. 2. Schematic instant wave profiles for two-dimensional liquid sloshing in a rectangular tank with horizontal excitation. Screen Sc_0 with $0 < Sn < 1$ in the middle is installed [part (a)]. Parts (b) and (c) illustrate the first antisymmetric wave profiles for the limit cases $Sn=0$ and $Sn=1$, respectively.

FIG. 3. Schematic response curves for a clean rectangular tank giving the steady-state resonance wave amplitude response A vs σ/σ^*_{2k-1} based on two-dimensional potential flow of an incompressible liquid. The dashed line shows results following from the linear sloshing theory. The solid lines represent response curves following from the nonlinear asymptotic theory, where the bold solid line notes stable steady-state solutions. A hysteresis effect is possible denoted by the points T, T_1, T_2, and T_3. The point i marks possibility of the secondary resonance whose concept for sloshing problem is elaborated and studied in detail by Faltinsen and Timokha (Ref. 5). The secondary resonance implies amplification of higher modes when a superharmonics becomes close to a higher natural sloshing mode. Depending on the nondimensional liquid depth h/l, we can have (a) soft-spring type behavior $(0.3368\ldots \lesssim h/l$ for $k=1$), or (b) hard-spring type behavior $(h/l \lesssim 0.3368\ldots$ for $k=1)$.

11). The effect of viscous boundary layers at the tank walls and bottom is assumed negligible (see Chap. 6 in Ref. 11)

Physically, there exist two limit cases associated with $Sn=0$ (no screen) and $Sn=1$ (solid central wall). Typical wave profiles are depicted in Fig. 2. Panels (b) and (c) are related to the lowest natural sloshing modes for the two limit cases. When $Sn=0$, the natural sloshing modes (within an arbitrary nonzero constant C_i) are expressed as

$$\varphi_i = \varphi_i^* = C_i \cos\left(\frac{\pi i}{l}(y+a)\right)\cosh(\pi i(z+h)/l),$$

$$\kappa_i = \kappa_i^* = \frac{\pi i}{l}\tanh\left(\frac{\pi i h}{l}\right), \quad \sigma_i^* = \sqrt{g\kappa_i^*}, \quad i=1,2,\ldots, \tag{3}$$

where σ_i^* are the corresponding natural sloshing frequencies (see Sec. 4.3.1.1 in Ref. 11). Expression (3) introduces symmetric (even, $i=2k$) and antisymmetric (odd, $i=2k-1$) modes. Inserting a slat-type screen at the tank middle does not change the symmetric natural modes, but the antisymmetric modes become discontinuous at the slats (So_0) and, therefore, cannot be described by expression (3).

Passage to $Sn=1$ leads to the central rigid wall dividing the whole tank into two equal symmetrically situated compartments. The corresponding natural sloshing modes in $Q_0^\pm$ are then defined by the formulas

$$\varphi_i^\pm = \varphi_i^{**\pm} = C_i \cos\left(\frac{\pi i}{a}(y \mp a)\right)\cosh(\pi i(z+h)/a),$$

$$\kappa_i = \kappa_i^{**} = \frac{\pi i}{a}\tanh\left(\frac{\pi i h}{a}\right), \quad \sigma_i^{**} = \sqrt{g\kappa_i^{**}}, \quad i=1,2,\ldots. \tag{4}$$

Because $l=2a$, $\sigma_i^{**}=\sigma_{2i}^*$, the case $Sn=1$ leads to vanishing of the natural sloshing frequencies responsible for the antisymmetric modes of the case $Sn=0$.

Faltinsen and Timokha[12] describe evolution of the antisymmetric natural sloshing modes from Eq. (3) to Eq. (4) as Sn changes from 0 to 1 with finite nondimensional depth h/l. These modes remain very close to Eq. (3) for $0 < Sn \lesssim 0.5$. The principal changes in the natural modes are detected in the range $0.5 \lesssim Sn < 1$.

2. Resonant steady-state response for a clean rectangular tank

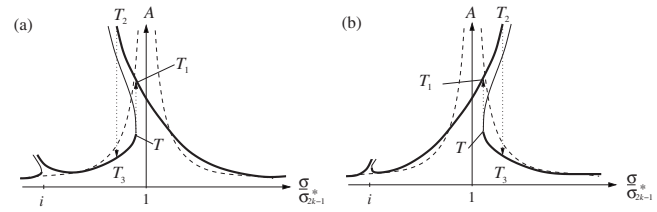Damping of liquid sloshing in a clean tank without wave breaking is small and mainly caused by the viscous boundary layer. Finite resonant harmonically excited liquid sloshing is mainly due to nonlinear transfer of energy between primary excited and higher modes. A review on the resonance steady-state wave amplitude response can be found in Chap. 8 of Ref. 11. According to asymptotic theory of nonlinear resonant steady-state sloshing, the *primary* resonance is only possible at the odd (antisymmetric) modes, i.e., when $\sigma \to \sigma^*_{2k-1}$. The corresponding response curves are schematically illustrated in Fig. 3. Depending on the nondimensional liquid depth, h/l, one can arrive at the soft-spring type response curves in the panel (a), or at the hard-spring type response curves in the panel (b). This change for the first resonance $\sigma \approx \sigma_1^*$ happens for asymptotically small η_{2a}/l at the critical depth $h/l=0.3368\ldots$. Nonlinear effects can also cause *secondary* resonances meaning that multiples of the forcing frequency is equal to a natural sloshing frequency.

B. Linear sloshing problem and the corresponding linear modal equations

1. Boundary value problem

Henceforth in our theoretical analysis, we *assume* that the liquid is inviscid and incompressible with irrotational flow except in a small vicinity of the screen where flow separation (or a jet flow) occurs. Let equation $z=\zeta(y,t)$ describe the free-surface elevations and $\Phi(y,z,t)$ be the absolute velocity potential defined in the tank-fixed coordinate system Oyz. The linear sloshing theory involves the Laplace equation and the boundary conditions coupling Φ and ζ:

$$\nabla^2\Phi = 0 \quad \text{in} \quad Q_0 = Q_0^+ \cup Q_0^-, \tag{5a}$$

$$\frac{\partial\Phi}{\partial y} = \dot{\eta}_2(t) \quad \text{on} \quad S_{0w}^\pm, \tag{5b}$$

$$\frac{\partial\Phi}{\partial z} = 0 \quad \text{on} \quad S_{0b}^\pm, \tag{5c}$$

$$\frac{\partial \Phi}{\partial z} = \frac{\partial \zeta}{\partial t} \quad \text{on} \quad \Sigma_0 = \Sigma_0^+ \cup \Sigma_0^-, \tag{5d}$$

$$\frac{\partial \Phi}{\partial t} + g\zeta = 0 \quad \text{on} \quad \Sigma_0 = \Sigma_0^+ \cup \Sigma_0^-, \tag{5e}$$

$$\int_{\Sigma_0} \zeta \, dy = 0. \tag{5f}$$

Geometric notations are explained in Fig. 1. The horizontal displacement of the tank is $\eta_2(t)$ and g is the gravity acceleration. Equations (5d) and (5e) are the linearized *kinematic* and *dynamic* boundary conditions formulated on the mean free surface $\Sigma_0 = \Sigma_0^- \cup \Sigma_0^+$.

The linear boundary problem Eq. (5) should be completed by appropriate boundary conditions on the screen Sc_0. When we *neglect* flow separation (or a jet flow) at the screen and, thereby, postulate the potential flow of an incompressible liquid everywhere in Q_0 including the openings Op_0, one should add the following linear boundary condition:

$$\frac{\partial \Phi}{\partial y} = \dot{\eta}_2 \quad \text{on} \quad So_0 \tag{6}$$

implying that the solid screen slats move horizontally together with the rectangular tank.

The problem Eqs. (5) and (6) require initial conditions which can be defined as

$$\zeta(y,0) = \zeta_0(y), \quad \frac{\partial \zeta}{\partial t}(y,0) = \zeta_1(y),$$

where ζ_0 and ζ_1 are the initial free-surface shape and velocity, respectively.

2. Linear modal solution when neglecting viscous screen effect

The linear sloshing problem Eqs. (5) and (6) have the following modal solution (see details in Chap. 5 of Ref. 11):

$$\zeta(y,t) = \sum_{i=1}^{\infty} \beta_i(t) f_i(y), \tag{7}$$

$$\Phi(y,z,t) = \dot{\eta}_2(t) y + \sum_{i=1}^{\infty} R_i(t) \varphi_i(y,z), \tag{8}$$

where $\varphi_i(y,z)[f_i(y) = \varphi_i(y,0)]$ are the natural sloshing modes appearing as the nontrivial eigensolution of the following spectral boundary problem:

$$\nabla^2 \varphi_i = 0 \quad \text{in} \quad Q_0; \quad \frac{\partial \varphi_i}{\partial n} = 0 \quad \text{on} \quad S_0 = S_{0w}^{\pm} \cup S_{0b}^{\pm} \cup So_0; \tag{9}$$

$$\frac{\partial \varphi_i}{\partial z} = \kappa_i \varphi_i \quad \text{on} \quad \Sigma_0.$$

The spectral parameter $\kappa_i > 0$ determines the natural sloshing frequencies

$$\sigma_i = \sqrt{g\kappa_i}, \quad i = 1, 2, \dots. \tag{10}$$

According to general theorems on the spectral boundary problem Eq. (9) (see, e.g., Refs. 16–18), the natural sloshing modes are orthogonal on Σ_0, i.e.,

$$\int_{\Sigma_0} f_i f_j \, dy = 0, \quad i \neq j; \quad f_i(y) = \varphi_i(y,0). \tag{11}$$

An accurate approximate eigensolution of the spectral problem Eq. (9) was constructed by Faltinsen and Timokha.[12] Analyzing this solution shows that the natural frequencies and modes are far from σ_{2i-1}^* for $0.5 \lesssim Sn < 1$. This means that, in contrast to earlier TLD analysis, we cannot adopt the eigensolution (3) for these solidity ratios.

The modal solution Eqs. (7) and (8) automatically satisfy all the relations of Eqs. (5) and (6) except the kinematic and dynamic boundary conditions Eqs. (5d) and (5e). Due to the orthogonality condition Eq. (11), the kinematic condition Eq. (5) couples $R_i(t)$ and $\beta_i(t)$ as follows:

$$R_i(t) = \frac{\dot{\beta}_i(t)}{\kappa_i}, \quad i = 1, 2, \dots. \tag{12}$$

After adopting Eq. (12) in the modal solution Eq. (8) and substituting this modal solution in the dynamic boundary condition Eq. (5d), the orthogonality condition Eq. (11) leads to the linear ordinary differential equations with respect to $\beta_i(t), i = 1, 2, \dots$, the so-called *linear modal equations*. For the considered tank shape, these modal equations take the form

$$\mu_k[\ddot{\beta}_{2k-1}(t) + \sigma_{2k-1}^2 \beta_{2k-1}(t)] + \lambda_k \ddot{\eta}_2(t) = 0, \quad k = 1, 2, \dots; \tag{13a}$$

$$\ddot{\beta}_{2k}(t) + \sigma_{2k}^2 \beta_{2k}(t) = 0, \quad k = 1, 2, \dots, \tag{13b}$$

where

$$\mu_k = \frac{1}{\kappa_{2k-1}} \int_{-a}^{0} f_{2k-1}^2 \, dy, \quad \lambda_k = \int_{-a}^{0} y f_{2k-1} \, dy, \quad k \geq 1. \tag{14}$$

We see that the η_2-forcing term is present only in Eq. (13a) responsible for antisymmetric modes, i.e., only antisymmetric modes are primary, directly excited. Symmetric modes depend in the linear approximation only on initial conditions. The hydrodynamic coefficients σ_{2i-1}, μ_k, and λ_k differ from similar coefficients in linear modal equations for sloshing in a clear rectangular tank (Chap. 5 in Ref. 11). Our hydrodynamic coefficients are now functions of Sn, the number of the submerged screen slots and their position.

C. Modification of the modal solution due to the pressure drop condition

The linear modal Eq. (13) must be modified to account for viscous cross-flow at the screen. The corresponding modification can be done by using a pressure drop condition at the screen. We will show, that this will lead to additional quadratic terms in the modal Eq. (13a) associated with the

antisymmetric modes. Because the symmetric modes do not cause cross-flow through the screen, the modal Eq. (13b) for symmetric modes will remain homogeneous within the framework of the linear sloshing theory.

1. Pressure drop condition

The pressure drop condition at the screen can be formulated as (see, e.g., Ref. 6)

$$P_- - P_+ = \tfrac{1}{2}\rho K u|u| \quad \text{on } \mathrm{Sc}_0, \qquad (15)$$

where K is an empirical pressure drop coefficient, ρ is the liquid density, u is the so-called *approach* velocity to the screen, and $(P_- - P_+)$ is the *pressure drop*. The pressure drop formulation Eq. (15) is based on that both sides of the screen are wetted. It does not apply in the free-surface zone where, due to different elevations at the screen sides, liquid goes through the openings to the dry screen side with further fall out. The falling liquid will then impact on the underlying free surface and thereby cause an extra dissipation.

The pressure drop coefficient K depends on the solidity ratio Sn. It may also depend on the Reynolds and Keulegan–Carpenter numbers. For slat-type screens, the pressure drop coefficient weakly depends on the Reynolds number (see details in Ref. 6, p. 314). Following Tait *et al.*[3] who referred to formulas by Baines and Peterson[19] and Weisbach,[20] we will adopt the following approximation of the empirical pressure drop coefficient

$$K = \left(\frac{1}{Cc(1 - \mathrm{Sn})} - 1 \right)^2,$$

$$(16)$$

$$Cc = 0.405 \exp(-\pi \mathrm{Sn}) + 0.595 \quad \text{for } \mathrm{Sn} \geq 0.3.$$

According to experimental studies by Tait *et al.*[3] for slat-type screens with Sn$=0.42$, different excitation frequencies close to the first natural sloshing frequency, and for intermediate and shallow liquid depths, formula (16) gives satisfactory approximation of K for the Keulegan–Carpenter number $KC = u_m T/D > 15$ where u_m is the amplitude of u, T is the oscillation period, and D is a characteristic length (here, the slot height). The pressure drop condition was originally formulated in the literature for uniform, coordinate-independent $u = u(t)$ and $P = P(t)$.

2. The horizontal approach velocity

The linear modal solution Eq. (8) based on the screen-modified natural sloshing modes following from the linear analysis by Faltinsen and Timokha[12] is assumed a first-order approximation of the relative horizontal velocity at the screen, i.e.,

$$U(y,z,t) = u(y,z,t) + \tilde{u}(y,z,t)$$

$$= \sum_{i=1}^{\infty} \frac{\dot{\beta}_{2i-1}(t)}{\kappa_{2i-1}} \frac{\partial \varphi_{2i-1}}{\partial y}(y,z), \quad y \neq 0, \qquad (17)$$

where φ_{2i-1} are the corresponding antisymmetric natural sloshing modes. Because dealing with the linear natural screen-modified sloshing modes by Faltinsen and Timokha[12] leads to a singular velocity field at the slot edges, the restric-

tion $y \neq 0$ is important; formally, U is infinite at these edges.

In expression (17), $\tilde{u}$ is the singular horizontal velocity component and u is the regular horizontal velocity component. The latter should be continuous at $y = 0$ so that $u(0, z, t)$ is associated with the approach velocity in formula (15). Because the natural sloshing modes are defined within an arbitrary nonzero multiplier C_{2i-1}, following Faltinsen and Timokha[12] leads to the expression

$$\varphi_{2i-1}(y,z) = C_{2i-1}(\phi_i(y,z) + \tilde{\phi}_i(y,z)), \quad i \geq 1, \qquad (18)$$

where the functions $\tilde{\phi}_i$ and ϕ_i are associated with $\tilde{u}(y,z,t)$ and $u(y,z,t)$, respectively. Furthermore, Ref. 12 shows that the functions $\phi_i(y,z)$ and $\tilde{\phi}_i(y,z)$ can be presented in a standard expansion adopted in many problems of the linear wave theory[13] and, therefore, take the form

$$\phi_i(y,z) = \mp \cosh(k_0^{(i)}(z+h)/a)\cos(k_0^{(i)}(y \mp a)/a), \quad (19a)$$

$$\tilde{\phi}_i(y,z) = \mp \sum_{j=1}^{\infty} A_j^{(i)} \cos(k_j^{(i)}(z+h)/a) \frac{\cosh(k_j^{(i)}(y \mp a)/a)}{\cosh(k_j^{(i)})}$$

$$\text{in } Q_0^\pm, \qquad (19b)$$

where $\{k_0^{(i)}, i \geq 1\}$ and $\{k_j^{(i)}, i \geq 1, j \geq 1\}$ are the roots of the equations

$$k_0^{(i)} \tanh(k_0^{(i)}h/a) = \kappa_{2i-1}a \quad \text{and} \quad k_j^{(i)} \tan(k_j^{(i)}h/a) = -\kappa_{2i-1}a,$$

$$(20)$$

$$i \geq 1, \quad j \geq 1.$$

Here, κ_{2i-1} are the eigenvalues of the spectral problem Eq. (9) in which the screen effect is included so that they are not equal to κ_{2i-1}^* in Eq. (3).

The terms associated with $\tilde{\phi}_i$ are evanescent terms exponentially decaying away from the screen; they capture the local singular character of the linear natural sloshing modes at the slot edges. The "wave components" of the natural sloshing modes, ϕ_i determines the surface wave profile and, thereby, the corresponding wave number $k_0^{(i)}$. It is very important that the wave numbers $k_0^{(i)}$ are mathematically not equal to the wave number of the corresponding clean tank, $\pi(2i-1)/l$. Faltinsen and Timokha[12] studied the screen effect on κ_{2i-1}, $k_0^{(i)}$, and $k_j^{(i)}$ as well as on the natural sloshing modes Eqs. (18) and (19). It follows from their analysis that the values $k_0^{(i)}$ are less than $\pi(2i-1)/l$ and $k_0^{(i)}$ monotonically decreases from $\pi(2i-1)/l$ to $2\pi(i-1)/l$ as Sn increases from 0 to 1. The values $k_0^{(i)}$ remain close to $\pi(2i-1)/l$ only for Sn ≤ 0.5, i.e., for a TLD-case. Furthermore, the values $k_j^{(i)}$ for lower natural sloshing modes rapidly tend to $\pi j/h$ as $j \to \infty$ providing almost zero flux through the screen associated with the function $\tilde{\phi}_i$.

The approach velocity u should represent the velocity flux through the screen without representing the local flow details (here, singularities at the edges) at the screen. This means that the approach velocity should be well approximated in terms of the "wave component" functions ϕ_i expressed by Eq. (19a). It follows from Eq. (17) that the approach velocity can then be determined by

$$u(z,t) = \sum_{i=1}^{N_m} \frac{\dot{\beta}_{2i-1}}{\kappa_{2i-1}} U_i(z), \quad -h < z < 0, \tag{21}$$

where N_m is the required number of antisymmetric modes $(N_m \to \infty)$ and

$$U_i(z) = \left. \frac{\partial \phi_i}{\partial y} \right|_{y=0} = -\frac{C_{2i-1}}{a} \cosh(k_0^{(i)}(z+h)/a)\sin(k_0^{(i)}). \tag{22}$$

3. The pressure drop condition and the modified modal equations

Using the linear modal solution Eq. (8) in expression for the dynamic pressure

$$p = -\rho \frac{\partial \Phi}{\partial t} \tag{23}$$

formally leads to a linear pressure drop at the slats, namely, $p_- - p_+ \neq 0$ on So_0 due to the discontinuous antisymmetric natural sloshing modes φ_{2i-1}. However, the difference $P_- - P_+$ in the pressure drop condition Eq. (15) has another physical nature. This pressure drop appears due to flow separation (or a jet flow) which is not captured by the linear modal solution.

We should first insert the approach velocity Eq. (21) into the pressure drop condition and find the corresponding pressure correction p_2. When expressing p_2, we use an analytical continuation of the irrotational flow to the whole liquid domain. Formally, this suggests the modified velocity potential

$$\Phi(y,z,t) = \dot{\eta}_2 y + \sum_{i=1}^{\infty} \frac{\dot{\beta}_i(t)}{\kappa_i} \varphi_i(y,z) \mp \frac{1}{\rho} \int_{t_0}^{t} p_2(y,z,t_1) dt_1$$

$$\text{in } Q_0^{\pm}. \tag{24}$$

Now, we should substitute Eqs. (7) and (24) into the problem Eq. (5) and satisfy the Laplace equation, the body-boundary condition, and the pressure drop condition $p_{2-} - p_{2+} = (1/2)\rho K u|u|$. Furthermore, we should also account for Eqs. (7) and (24) into kinematic Eq. (5d) and dynamic Eq. (5e) boundary conditions. The latter conditions (see Appendix A) give

$$\frac{\partial p_2}{\partial n} = 0 \quad \text{on } \Sigma_0^{\pm}, \tag{25a}$$

$$\ddot{\eta}_2 y + \sum_{i=1}^{\infty} \frac{\ddot{\beta}_i(t) + g\kappa_i \beta(t)}{\kappa_i} f_i(y) \mp \frac{1}{\rho} p_2(y,0,t) = 0$$

$$\text{on } \Sigma_0^{\pm}. \tag{25b}$$

It may look unphysically that, as the derivations in Appendix A show, the pressure-correction term p_2 satisfies the Neumann boundary condition Eq. (25a) on the mean free surface. However, one should remember the specific definition of p_2 in the modified velocity potential Eq. (24) implying that the integral over p_2 is also a correction of the velocity potential. The latter gives Eq. (A3) following from the kinematic condition Eq. (5d), and because Eq. (A3) is true

for any instant t, one mathematically gets the zero-Neumann condition Eq. (25a) for the pressure-correction term.

Using Eq. (25a) together with relations in Eq. (A1) and the pressure drop condition leads to the boundary value problem

$$\nabla^2 p_2 = 0 \quad \text{in } Q_0^{\pm};$$

$$\frac{\partial p_2}{\partial n} = 0 \quad \text{on } S_{0b}^{\pm} \cup S_{0w}^{\pm} \cup \Sigma_0^{\pm}; \tag{26}$$

$$p_2 = \pm \frac{1}{4} \rho K u |u| \quad \text{on } Sc_0.$$

This problem has the following solution

$$p_2 = \pm \rho \frac{K}{4h} \left(\Omega_0 + 2 \sum_{k=1}^{\infty} \Omega_k \cos\left(\frac{\pi k}{h} z\right) \frac{\cosh(\pi k(y \mp a)/h)}{\cosh(\pi k a/h)} \right), \tag{27}$$

where

$$\Omega_k = \int_{-h}^{0} u|u| \cos\left(\frac{\pi k}{h} z\right) dz, \quad k \geq 0. \tag{28}$$

One must note that when introducing the approach velocity via Eq. (21) we neglect the evanescent terms exponentially decaying away from screen which are responsible for a singular character of the linear natural sloshing modes at the slot edges. We see that similar exponentially decaying terms appear in solution Eq. (27) associated with $\Omega_k, k \geq 1$. These terms do not contribute to the screen averaged pressure, but are only responsible for a local nearly screen change of the pressure field by p_2. This local change has no physical meaning, especially for larger k because the local field at the screen is in reality viscous. Excluding these exponentially decaying terms means an averaged (over the mean screen height) pressure drop which will furthermore be adopted. The modified velocity potential Eq. (24) should then be approximated by

$$\Phi(y,z,t) = \dot{\eta}_2 y + \sum_{i=1}^{\infty} \frac{\dot{\beta}_i(t)}{\kappa_i} \varphi_i(y,z)$$

$$\mp \frac{K}{4h} \int_{t_0}^{t} \left(\int_{-h}^{0} u(z,t_1)|u(z,t_1)| dz \right) dt_1 \quad \text{in } Q_0^{\pm}, \tag{29}$$

where u is given by Eq. (21).

Let us consider the dynamic Eq. (25b) and use the orthogonality Eq. (11). This gives the modified modal equations with respect to β_{2i-1}

$$\mu_k(\ddot{\beta}_{2k-1}(t) + \sigma_{2k-1}^2 \beta_{2k-1}(t)) + \lambda_k \ddot{\eta}_2(t)$$

$$- \frac{K\alpha_k}{4h} \int_{-h}^{0} \left(\sum_{i=1}^{N_m} \frac{\dot{\beta}_{2i-1}}{\kappa_{2i-1}} U_i(z) \right) \left| \sum_{i=1}^{N_m} \frac{\dot{\beta}_{2i-1}}{\kappa_{2i-1}} U_i(z) \right| dz = 0,$$

$$k = 1, 2, \ldots, N_m, \tag{30}$$

where N_m is the required number of antisymmetric modes [also see Eq. (21)], and

$$\alpha_k = \int_{-a}^{0} f_{2k-1}(y)\mathrm{d}y. \qquad (31)$$

Other hydrodynamic coefficients are expressed by Eqs. (10) and (14). The symmetric modes are governed by Eq. (13b), i.e., they are not excited by the horizontal forcing $\eta_2(t)$ within the framework of the linear free-surface theory.

Based on studies by Faltinsen and Timokha[12] for a uniformly slotted screen with $0.5 \lesssim \mathrm{Sn} < 0.95$ and relatively small number of the openings $N \lesssim 50$, the natural sloshing frequencies and modes and, therefore, the hydrodynamic coefficients κ_i, σ_i, μ_i, λ_i, and α_i become strongly dependent on the geometric dimensions of the mean liquid domain, h and l, and, in addition, on the *two independent* screen parameters Sn and N. The hydrodynamic coefficients can also change with the position of the slot nearest to the mean free surface, i.e., due to the fact that the slot goes in and out of the mean free surface. When $0 < \mathrm{Sn} \lesssim 0.5$, the natural sloshing modes and frequencies are close to those for the clean tank and the latter additional dependencies can be neglected.

Henceforth, we consider steady-state liquid sloshing occurring due to the harmonic sway excitation $\eta_2(t) = \eta_{2a}\cos(\sigma t)$, where η_{2a} is the forcing amplitude, and σ is the forcing frequency. The emphasis will be on the η_{2a}-scaled wave elevations which, according to the modal presentation Eq. (7), is described by the formula

$$\zeta^*(y,t) = \sum_{i=1}^{\infty} \beta_i^*(t)f_i(y), \quad \beta_i^*(t) = \beta_i(t)/\eta_{2a}. \qquad (32)$$

When l (tank width) is the characteristic size and $1/\sigma$ is the characteristic time, the modal Eqs. (30) can be rewritten to the nondimensional form with respect to $\beta_i^*(t)$:

$$\bar{\mu}_k(\ddot{\beta}_{2k-1}^*(t) + \bar{\sigma}_{2k-1}^2\beta_{2k-1}^*(t)) - \bar{\lambda}_k\cos t$$

$$- [K\bar{\eta}_{2a}]\frac{\bar{\alpha}_k}{4\bar{h}}\int_{-\bar{h}}^{0}\left(\sum_{i=1}^{N_m}\frac{\dot{\beta}_{2i-1}^*}{\bar{\kappa}_{2i-1}}\bar{U}_i(\bar{z})\right)$$

$$\times \left|\sum_{i=1}^{N_m}\frac{\dot{\beta}_{2i-1}^*}{\bar{\kappa}_{2i-1}}\bar{U}_i(\bar{z})\right|\mathrm{d}\bar{z} = 0, \quad k = 1,2,\ldots,N_m, \qquad (33)$$

where we have introduced the nondimensional parameters

$$\bar{\sigma}_i = \sigma_i/\sigma, \quad \bar{\eta}_{2a} = \eta_{2a}/l, \quad \bar{U} = lU,$$

$$\bar{\kappa}_i = \kappa_i l, \quad \bar{h} = h/l, \quad \bar{z} = z/l,$$

$$\bar{\mu}_i = \mu_i/l^2, \quad \bar{\lambda}_i = \lambda_i/l^2, \quad \bar{\alpha}_i = \alpha_i/l.$$

When σ/σ_1^* and h/l are constant values, $0.5 \lesssim \mathrm{Sn}$, and $N \lesssim 50$, the steady-state solution of Eq. (33) strongly depends on the nondimensional parameter $[K\bar{\eta}_{2a}]$ (in the front of the integral term), the independent parameters Sn, N, and, generally, the position of the slot closest to the mean free surface. This is because, as we remarked above, all these input parameters can change the hydrodynamic coefficients in the
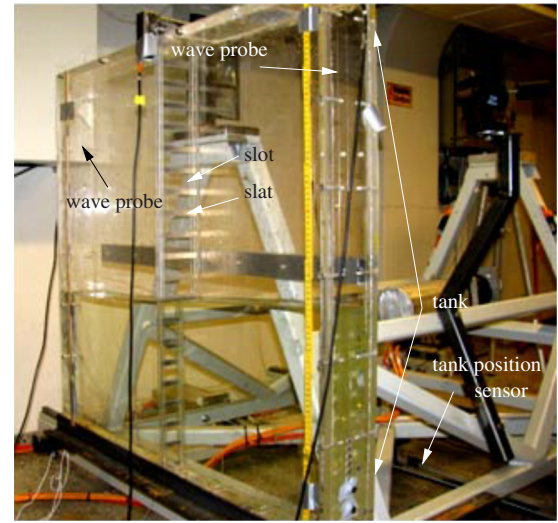

FIG. 4. (Color online) Experimental set-up and equipments.

modal equations. A simplification comes for *smaller solidity ratios*, $0 < \mathrm{Sn} \lesssim 0.5$ and $10 \lesssim N$ when (Ref. 12) the natural sloshing modes and frequencies (and the corresponding hydrodynamic coefficients) are close to those for the clean tank and, therefore, the steady-state solution of Eq. (33) is only function of σ/σ_1^*, h/l, and the nondimensional parameter $[K\bar{\eta}_{2a}]$. Another simplification is possible for a *porous-media screen* implying the *limit case $N \to \infty$*. During preparation of Ref. 12, the authors established that, whereas $100 \lesssim N$ and $0.5 < \mathrm{Sn} < 0.95$, the natural sloshing frequencies and modes become only functions of Sn [or K because one can define $\mathrm{Sn} = \mathrm{Sn}(K)$ by inverting the monotonic function Eq. (16)]. Thus, the porous media limit implies that the steady-state solution of Eq. (33) depends on the independent nondimensional input parameters σ/σ_1^*, h/l, $K\bar{\eta}_{2a}$, and K.

The periodic steady-state solution has been found from the system Eq. (30) by numerical time-integration following a fifth-order Runge–Kutta method with arbitrary initial conditions associated with initial free-surface shape and velocity. This becomes possible because the modal equations imply a dissipative mechanical system, i.e., transient waves die out with increasing time.

III. EXPERIMENTS

A Plexiglas-made rectangular tank was installed in a rig located at the Marine Technology Center in Trondheim, Norway. The tank's internal dimensions are $1.0~\mathrm{m} \times 0.98~\mathrm{m} \times 0.1~\mathrm{m}$ (width $\times$ height $\times$ breadth). The setup photograph is shown in Fig. 4. The tank has been equipped with two resistant wave probes. The measurement accuracy of the wave elevations is about 1 mm. The measurement probes have been installed at 1 cm away from the two opposite vertical walls. Two considerations determined our choice of the tank breadth. One is that we wanted to achieve two-dimensional flow conditions and, hence, the breadth-to-width ratio has to be small. The other criterion is that the tank breadth must be clearly larger than the boundary layers at the tank walls and the thin side-screen bracings "B" of 0.005 m (see Fig. 5).
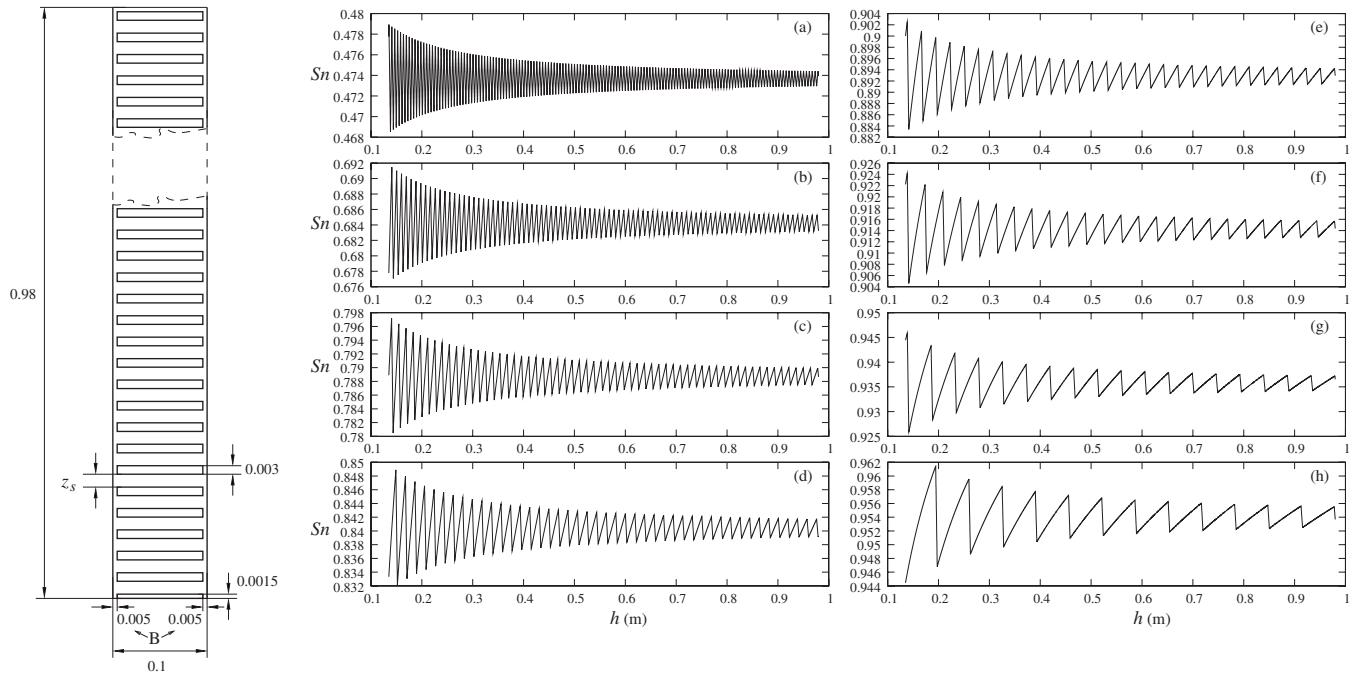
FIG. 5. Geometric parameters of the perforated plate (screen). All the numerical values are in meters. The plate thickness is 5 mm. The distance between the two nearest slots, z_s, takes the values $z_s = 0.0027$ m (screen a), 0.0065 m (screen b), 0.0112 m (screen c), 0.0158 m (screen d), 0.025 m (screen e), 0.032 m (screen f), 0.0437 m (screen g), and 0.0623 m (screen h). Due to technical limitations in the drilling of the slots, the minimum possible slot height 3 mm was used for all the screens. This causes eight different solidity ratios which, generally, change with the liquid depth as shown in panels (a)–(h). Effect of the rigid side-screen bracings B of 0.005 m width is neglected in our analysis.

Meniscus effects occur at the intersection between the tank walls and the free surface leading to three-dimensional waves with very small wave height and wavelength relative to the gravity waves. The error due to meniscus effects is believed negligible.

The plate with perforated slots is mounted in the tank middle (see Fig. 4). The plate thickness is 5 mm which is neglected in our theoretical model. The geometric structure of the perforated plate is illustrated in Fig. 5. Due to technical limitations in the drilling of the slots, the minimum possible slot height 3 mm was used for all the screens (a)–(h). It has been controlled that the slot height is very close to constant through the screen. If that was not the case, it could cause a bias in the sloshing in the two compartments. The latter fact was observed by originally using wrongly manufactured screens. For larger solidity ratios, there is only a limited number of slots below the free surface.

Forced lateral harmonic tank motion $\eta_2 = \eta_{2a} \cos(\sigma t)$ is studied. The steady-state wave elevation at the walls is recorded for different forcing frequencies in specified frequency intervals. Because the shallow-liquid sloshing is not adequately described by the linear sloshing theory except for very small excitation amplitudes, our focus in the present paper is on finite liquid depths. The frequency range is $[\approx 0.6$ Hz, ≈ 1.7 Hz$]$ which includes the required resonance frequencies $\sigma_1^*/2\pi$, $\sigma_2^*/2\pi$, and $\sigma_3^*/2\pi$ [see Eq. (3)] of the corresponding clean tank for the tested liquid depths 0.4 and 0.35 m. An important consideration was to avoid tank roof impact which would lead to an extra energy dissipation (see Chap. 11 in Ref. 11). The latter fact implied that η_{2a}/l was

limited to slightly higher than 0.01 in tests with the 0.4 m liquid depth.

In the experiments, the model tests started with the largest test frequency. The forcing frequency was subsequently decreased and kept fixed for a certain time interval. The reason for decreasing the forcing frequency is to detect the maximum wave elevation. The latter fact follows from the possible soft-spring type nonlinear steady-state response for a smooth two-dimensional rectangular tank with the tested finite liquid depths (see Fig. 3). Each experimental series with a fixed forcing frequency lasted, normally, for about 300 cycles. Some isolated tests were made with 400–500 cycles to confirm that the experimentally found steady-state conditions remain stable on a long-time scale. The wave elevation usually reached the experimental steady-state condition after about 80–200 cycles and then the maximum wave-elevation in the steady-state region is found. Then the forcing frequency switched to a lower value and, again, to reach the next steady-state responses. The step of frequency changes is smaller around the peak points of the response in order to have the precise value of the resonance frequencies. The wave elevation is recorded with a sampling rate of 100 Hz and measured relative to the unperturbed free surface.

IV. COMPARISON WITH EXPERIMENTS

For screens (a)–(h) in Fig. 5 and $h/l = 0.4$, the corresponding solidity ratios are computed to be Sn = 0.4725, 0.6825, 0.786 25, 0.838 75, 0.891 25, 0.913 75, 0.936 25, and 0.951 25 with $N = 70$, 42, 29, 22, 15, 12, 9, and 7, re-

spectively. Formula (16) gives the corresponding pressure drop coefficients, $K=3.09862$, 15.2292, 41.4063, 79.8816, 191.550, 315.503, 597.750, and 1045.40. The forcing amplitudes were $\eta_{2a}/l \approx 0.001$ and 0.01.

The larger forcing amplitude $\eta_{2a}/l=0.03$ was used for the model tests with $h/l=0.35$. For this liquid depth, the solidity ratios are Sn=0.472857, 0.687 143, 0.790, 0.841 429, 0.892 857, 0.914 286, 0.935 714, and 0.952 857 with $N=62$, 37, 25, 19, 13, 10, 8, and 6, respectively. The pressure drop coefficients are then evaluated by formula (16) to be $K=3.10666$, 15.8448, 43.1960, 82.9828, 197.846, 319.727, 587.348, and 1120.55, respectively.

The tested forcing frequency range covers the lower natural sloshing frequencies σ_1^*, σ_2^* and σ_3^*. For $h/l=0.4$, the ratios between these frequencies are $\sigma_2^*/\sigma_1^*=1.524$ and $\sigma_3^*/\sigma_1^*=1.878$ with $\sigma_1^*=5.119$ (rad/s). For $h/l=0.35$, $\sigma_2^*/\sigma_1^*=1.561$, and $\sigma_3^*/\sigma_1^*=1.933$ with $\sigma_1^*=4.966$ (rad/s).

For all the experimental input parameters, the Runge–Kutta integrations by Eq. (30) showed a fast convergence in terms of the modal system dimension N_m. Four modal equations of Eq. (30), $N_m=4$, provided stabilization of four-five significant figures of the numerical steady-state wave elevations. This means that, according to the quasilinear modal theory, the global liquid motions are well described by the four lower antisymmetric sloshing modes for the considered frequency range.

A. Experiments with the lowest forcing amplitude $\eta_{2a}/l \approx 0.001$ and $h/l=0.4$

Comparison of the measured maximum steady-state wave elevations at the walls (1 cm away) and our theoretical prediction by the modal system Eq. (30) is shown in Fig. 6. The solid circles (●) denote the experimental values, but the solid lines represent the corresponding theoretical values. In the figure, these values are scaled by the forcing amplitude η_{2a}. Generally, the experimental forcing amplitudes were different (up to a 10%-change) for different forcing frequencies. This is illustrated by the narrow horizontal graphs beneath the panels (a)–(h) in Fig. 6. The calculations by our quasilinear theoretical model Eq. (30) accounted for the actual experimental values of η_{2a}.

Results by the quasilinear theory is in very good agreement with experiments in the panels (b)–(g) of Fig. 6. A flat-type experimental response for certain frequency ranges in the panels (e)–(f) may be due to the measurement error of about 1 mm. In these frequency ranges, variations of the theoretical response curves are comparable with this error.

In the panels (a)–(f), we see the two resonant peaks associated with the natural frequencies σ_1 and σ_3 (and the corresponding modes φ_1 and φ_3) which remain relatively close to σ_1^* and σ_3^*. The theoretical peak at σ_3 is always higher than the similar peak at σ_1. This is explained by the fact that the natural sloshing mode φ_3 [see its dominant component Eq. (19a)] provides a faster decay from the mean free surface to the bottom and, thereby, leads to a lower cross-flow. The lower cross-flow through the screen for $\sigma \approx \sigma_3^*$ implies a lower damping due to flow separation (or jet flow) and a larger wave amplitude response is, therefore, expected.

Figure 6(a) shows discrepancies for the smallest tested solidity ratio Sn=0.4725. First, we see a drift of the experimental peaks to the left of their theoretical expectations. Second, as we have explained above by the decreased cross-flow through the screen, the theoretical wave elevations at $\sigma \approx \sigma_3$ should be higher of those at $\sigma \approx \sigma_1$ but the experimental values do not confirm that. Because the experimental and theoretical maximum wave elevations at the resonant peaks are, at least, 25-times larger than the forcing amplitude, the discrepancies can be explained by the free-surface nonlinearity leading to a soft-spring type response outlined in Sec. II A 2. Furthermore, effect of the free-surface nonlinearity is more important at $\sigma \approx \sigma_3$ because, as we stated, the screen-caused damping is of less importance for the second primary-excited resonance.

The free-surface nonlinearity mechanism explains also the difference between the quasilinear theoretical prediction and experimental measurements in the panel (h) with Sn =0.95125 ($K=1045.45$). For this solidity ratio, the screen almost (but not completely) prevents the cross-flow between compartments Q_0^+ and Q_0^- so that the free-surface motions are similar to those in Fig. 2(c), i.e., they occur almost independently in Q_0^+ and Q_0^- alike in the two corresponding clean tanks with the liquid depth-to-width ratio $h/a=0.8$. The non-linear soft-spring behavior of the response curves is then expected (see Sec. II A 2). However, sloshing in the panel (h) cannot be modeled as fully *independent* resonant wave motions in two compartments Q_0^+ and Q_0^- with a rigid wall between them. Assuming independent sloshing in the compartments with *zero* cross-flow at the screen implies that $\sigma_3 \approx \sigma_2^*$ and, therefore, we should expect the linear response peak at $\sigma/\sigma_2^* \approx 1.524$ and the nonlinear resonance peak should, due to the soft-spring behavior, be to the left of this value. The panel (h) does not confirm such positions of these peaks. This means that cross-flow is still not completely zero and we arrive at the situation where both the cross-flow and the free-surface nonlinearity matter.

The theoretical-and-experimental results in Fig. 2 help judging on the general trends of the steady-state resonance response curves with increasing Sn in the range $0.5 \lesssim$ Sn $\lesssim 0.95$:

- For the smaller solidity ratios Sn=0.4725, 0.6825, 0.786 25, and 0.83875, the steady-state resonance response in panels (a)–(d) shows two clear resonance peaks associated with the two lowest antisymmetric modes. The peaks remain close to $\sigma/\sigma_1^* \approx 1$ and $\sigma/\sigma_1^* \approx 1.878$, i.e., they occur in a neighborhood of the natural sloshing frequencies Eq. (3). Furthermore, the maximum nondimensional wave elevations in the considered frequency range becomes smaller with increasing Sn. This means that increasing Sn between ≈ 0.5 and ≈ 0.85 increases the global damping in the mechanical system.

- Figures 6(e) and 6(f) with Sn=0.891 25 and 0.913 75 shows that further increase of the solidity ratio leads to an increase of the global damping at $\sigma/\sigma_1^* \approx 1$, but the theoretical and experimental steady-state resonance response at the second resonance peak (associated with
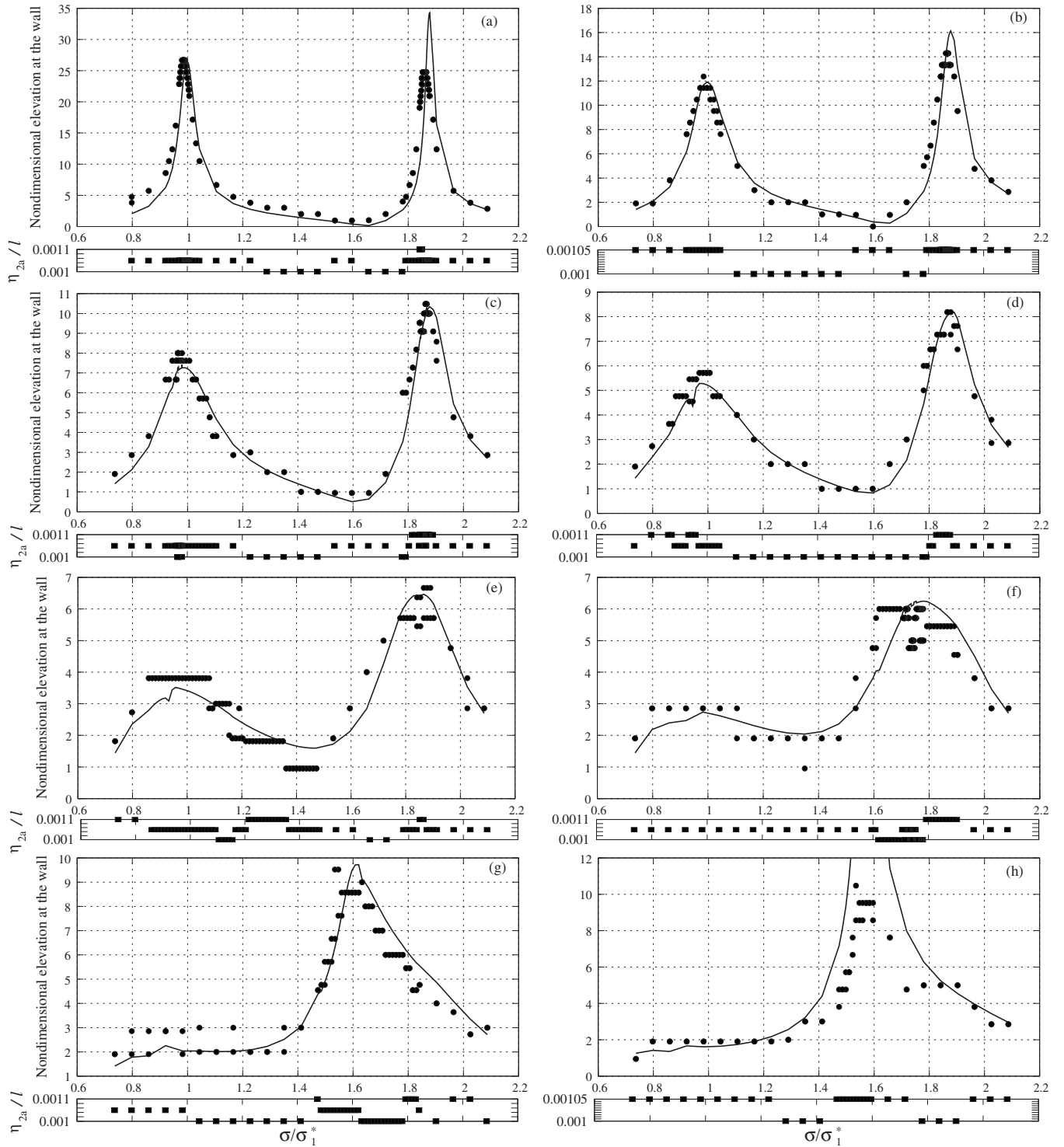
FIG. 6. The nondimensional experimental (●) and theoretical (solid line) maximum steady-state wave elevations at the vertical wall (at the two measurement probes situated 1 cm away from the wall) vs the forcing frequency; $h/l=0.4$. The wave elevations are scaled by the forcing amplitude η_{2a}, but the forcing frequency σ is scaled by the lowest natural sloshing frequency for the clean tank (3). The nondimensional forcing amplitude η_{2a}/l is about 0.001. Change of η_{2a}/l vs σ/σ_1^* for experimental series is shown. The change is accounted for in the computations by the modal Eqs. (30). (a) Sn=0.4725, $N=70$, $K=3.09862$, (b) Sn=0.6825, $N=42$, $K=15.2292$, (c) Sn=0.78625, $N=29$, $K=41.4063$, (d) Sn=0.83875, $N=22$, $K=79.8816$, (e) Sn=0.89125, $N=15$, $K=191.550$, (f) Sn=0.91375, $N=12$, $K=315.503$, (g) Sn=0.93625, $N=9$, $K=597.750$, (h) Sn=0.95125, $N=7$, $K=1045.40$.

the second antisymmetric mode) remains almost the same. Furthermore, we see a drift of this second resonance peak to the left of $\sigma/\sigma_1^* \approx 1.878$, i.e., from 1.87 to 1.75.

• Changing the solidity ratio to 0.936 25 in the panel (g)

leads to vanishing of the first resonance peak, but the second resonance peak occurs at $\sigma/\sigma_1^*=1.6$. The largest tested solidity ratio 0.951 25 in the panel (h) theoretically shows a clear linear resonance at $\sigma/\sigma_1^*=1.59$. The maximum theoretical η_{2a}-scaled wave el-
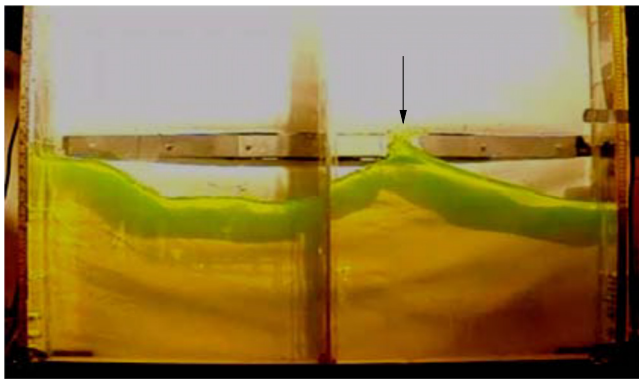
FIG. 7. (Color online) Typical wave breaking occurring for all the tested solidity ratios Sn $\lesssim$ 0.9 in the range of 1.25 $< \sigma/\sigma_1^* <$ 1.78 for the model tests with $h/l=0.4$ and $\eta_{2a}/l \approx 0.01$. The photograph and video recording are for the screen (a) with Sn=0.481 25 and the forcing frequencies $\sigma/\sigma_1^*=1.71$ and 1.75, respectively (enhanced online). [URL: http://dx.doi.org/10.1063/1.3562310.1]

evation is computed to be about 40; it is not shown in the panel. Instead, experiments give much lower values with a local peak at $\sigma/\sigma_1^*=1.54$ which has earlier been explained by a complex effect due to nonlinear soft-spring type behavior and non-negligible cross-flow through the screen.

B. Increasing the forcing amplitude to $\eta_{2a}/l=0.01$ with $h/l=0.4$

Increasing the forcing amplitude to $\eta_{2a}/l=0.01$ leads to a set of specific free-surface phenomena documented by means of photographs and videos in Figs. 7–12 These phenomena are mainly observed in the frequency range 1.25 $< \sigma/\sigma_1^* <$ 1.78 and, for the screen (a) with the smallest tested solidity ratio 0.4725, in the range 0.92 $\lesssim \sigma/\sigma_1^* \lesssim$ 1.04. The free-surface phenomena can be classified in the following way:

- *Wave breaking* (basically of spilling type) happens for all the tested solidity ratios Sn $\lesssim$ 0.9 in the range of 1.25 $< \sigma/\sigma_1^* <$ 1.78. It is most severe for lower Sn. Figure 7 exhibits the corresponding photograph and

FIG. 9. (Color online) A typical three-dimensional perturbations of the free surface occurring for 0.7 $\lesssim$ Sn $\lesssim$ 0.9 and 1.66 $\lesssim \sigma/\sigma_1^* \lesssim$ 1.73; $h/l=0.4$, $\eta_{2a}/l \approx 0.01$. The video is for the screen (b) with Sn=0.6825 and σ/σ_1^* =1.72 (enhanced online). [URL: http://dx.doi.org/10.1063/1.3562310.2]

video for the screen (a) with $\sigma/\sigma_1^*=1.71$ and σ/σ_1^* =1.75, respectively. The wave breaking occurs periodically in the left and right compartments as a consequence of collision between cross-flow going from the screen and an incoming wave in the corresponding compartment. For the screen (a) with the lowest tested solidity ratio, a local wave breaking is also observed for $\sigma/\sigma_1^* \approx 0.98$ as it is seen in Fig. 8. The latter disappears for other screens with higher solidity ratios.

- For 0.7 $\lesssim$ Sn $\lesssim$ 0.9, we established *three-dimensional* wave motions in the frequency range 1.66 $\lesssim \sigma/\sigma_1^*$ $\lesssim$ 1.73. Figure 9 displays the corresponding video for the screen (b) with Sn=0.6825 and $\sigma/\sigma_1^*=1.72$. These three-dimensional waves are accompanied by a local wave breaking. We were not able to identify what kind of cross-wave resonance causes the observed three-
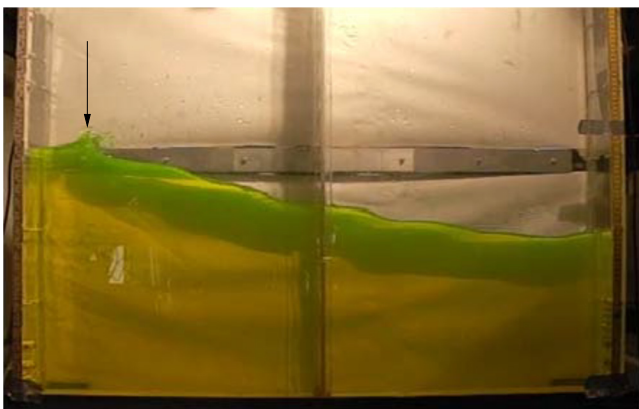

FIG. 8. (Color online) Local wave breaking occurring for the screen (a) with $\sigma/\sigma_1^* \approx 0.98$, $h/l=0.4$, and $\eta_{2a}/l=0.01$.
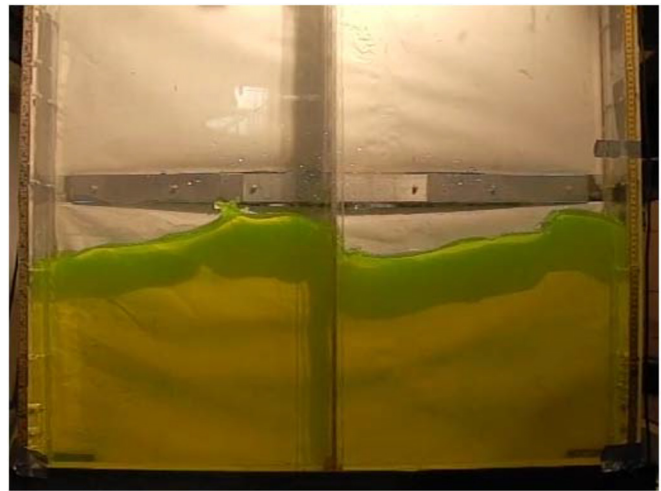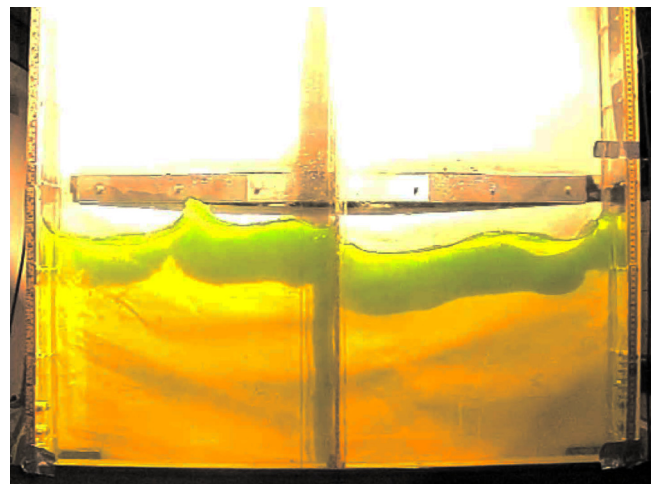

FIG. 10. (Color online) Video recording of a steep wave with the double superharmonics elevations at the walls (enhanced online). [URL: http://dx.doi.org/10.1063/1.3562310.3]
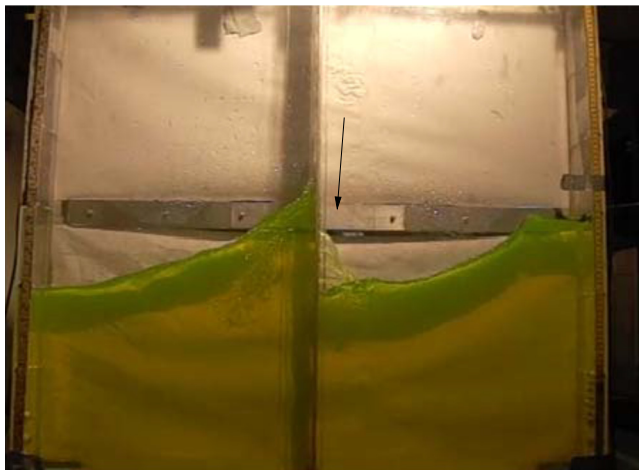
FIG. 11. (Color online) Photo of the liquid jet through the screen for Sn $=0.891\,25$ and $\sigma/\sigma_1^*=1.48$.

dimensional waves. A dedicated study in the manner of Faltinsen *et al.* is needed.[21]

- The video in Fig. 10 illustrates the second Fourier harmonics for the nearly wall wave elevations established in our visual observations for the screens (b)–(d). In addition, these cases are characterized by steep wave patterns. The latter fact indicates an amplification of higher sloshing modes. Mechanism of this amplification in sloshing problems consists of the secondary resonance yielding the energy content from a primary-excited mode to higher modes via the free-surface nonlinearity (see Chap. 8 in Ref. 11).

- Liquid jets through the screen openings over the free surface with subsequent fallout on the opposite free surface happened for the screens (e)–(h) in a frequency range about $\sigma/\sigma_1^*=1.524$. Figure 11 shows the jet for the screen (c) and $\sigma/\sigma_1^*=1.48$.

- Runup with a detachment of a liquid portion along the screen happened for the solidity ratios $0.9 \lesssim \mathrm{Sn}$. Figure 12 shows the corresponding photograph and video.

Even though the aforementioned surface phenomena in-

FIG. 12. (Color online) The photograph and video recording of the runup at the screen occurring for $0.9 \lesssim \mathrm{Sn}$ (enhanced online).[URL: http://dx.doi.org/10.1063/1.3562310.4]

dicate importance of the free-surface nonlinearity, we used the quasilinear modal theory to describe the steady-state wave elevations at the walls. The results are compared with experimental values in Figs. 13 and 14.

Figures 6(a)–6(d) and 13 demonstrate that increasing the forcing amplitude leads to the experimental response curves which cannot be fully quantified by the quasilinear theory. The reasons are (i) additional resonance peaks about the vertical dashed lines; (ii) a nonlinear soft-spring type behavior in a frequency range covering the natural sloshing frequency σ_3.

When considering Fig. 13(a) with the lowest tested Sn $=0.4725$ and comparing it with Fig. 6(a), a much clearer soft-spring behavior of the experimental amplitude response occurs at $\sigma \approx \sigma_3^*$. The experimental resonance peak at the first natural frequency, $\sigma \approx \sigma_1^*$, remains in these figures of a linear character. Recalling that the aforementioned lower cross-flow through the screen by the natural mode φ_3 (associated with exponential decay to the bottom) leads to a lower screen-caused damping clarifies a stronger effect of the free-surface nonlinearity which should yield for the tested liquid depth the soft-spring type response curve. Our quasilinear theory cannot capture this response as well as it cannot describe amplification of higher harmonics. However, it remains applicable for prediction of the first Fourier harmonics contribution in a local neighborhood of $\sigma \approx \sigma_1^*$ in Figs. 13 and 14. The vanishing of the first resonance peak with increasing *Sn* is reasonably well predicted. This occurs for Sn$=0.786\,25$ [screen (c)] while the lower forcing amplitude detected this vanishing only for Sn$=0.936\,25$ [screen (g)].

Figures 13 and 14 show that the quasilinear theory is, generally, not applicable in the frequency range $1.1 \lesssim \sigma/\sigma_1^* \lesssim 1.9$ for quantification of the steady-state amplitude response. It describes only a general trend of the maximum resonance peak position versus Sn. In the middle of this frequency range, $1.3 \lesssim \sigma/\sigma_1^* \lesssim 1.78$, experimental observations establish the aforementioned specific free-surface phenomena which are of a clear nonlinear nature. Being invalid in modeling the free-surface nonlinearity, the quasilinear theory shows in Fig. 14 a linear-type amplitude response about σ_3 (note that this natural sloshing frequency decreases from σ_3^* to σ_2^* as Sn tends to 1) while the experimental measurements show a soft-spring type response curves at the same frequency. For smaller forcing amplitude in Fig. 6, this kind of discrepancies was detected only for the maximum tested solidity ratio Sn$=0.951\,25$.

Remembering the video in Fig. 10 detecting the double Fourier harmonics, we present in Figs. 13 and 14 the η_{2a}-scaled contributions of the first ($\triangle$) and second (∇) Fourier harmonics components of the $2\pi/\sigma$-periodic measured steady-state signal. The sum of the first and second harmonics contributions in the figures gives approximately the actual wave elevation for almost all the experimental data and, therefore, relates appearance of the additional peaks to amplification of second harmonic response. Since the $(\cdot|\cdot)$-nonlinearity can only yield odd harmonic terms, the existence of the second Fourier harmonics cannot be explained within the framework of the quasilinear theory. To explain amplification of the second Fourier harmonics, we
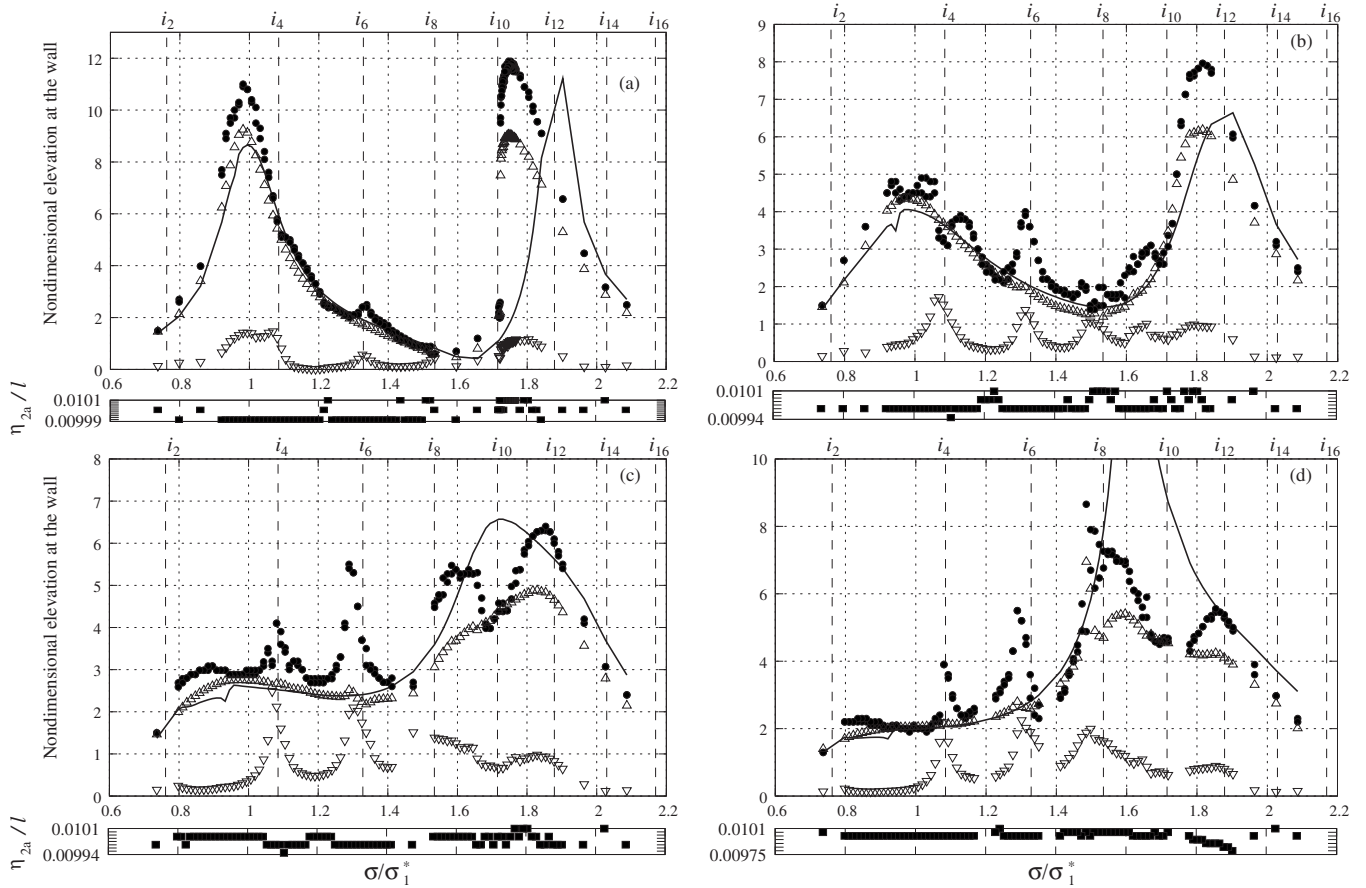
FIG. 13. The same as for the panels (a)–(d) in Fig. 6, but for the larger forcing amplitude $\eta_{2a}/l \approx 0.01$. Contribution of the first Fourier harmonics to the measured wave elevations (scaled by η_{2a}) is denoted by $\triangle$, but $\triangledown$ denotes contribution of the second Fourier harmonics. The values $\sigma/\sigma_1^* = i_{2k}, k \geq 1$ [see Eq. (34) and the corresponding vertical dashed lines] indicate the frequencies where the secondary resonance due to the second-order free-surface nonlinearity is expected.

should implement the adaptive multimodal analysis elaborated by Faltinsen and Timokha.[5] According to this analysis, the second Fourier harmonics in the steady-state sloshing solution can only be resonantly excited due to the second-order free-surface nonlinearity when the forcing frequency is close to the one-half of the corresponding natural frequency of a symmetric mode, i.e., $2\sigma \approx \sigma_{2k}, k \geq 1$. The latter condition leads to

$$\frac{\sigma}{\sigma_1^*} \approx \frac{\sigma_{2k}^*}{2\sigma_1^*} = i_{2k}. \qquad (34)$$

Figure 13 shows that the values $\sigma/\sigma_1^* = i_{2k}$, $k=1$, 2, 3, 4, and 5 well predict the frequencies of the resonance peaks associated with the second Fourier harmonics amplification.

C. Experiments with $\eta_{2a}/l = 0.03$ and $h/l = 0.35$

Increasing the forcing amplitude makes the previously described above free-surface phenomena much more severe. Along with very strong wave breaking and runup, we observed overturning waves and formation of gas pockets. A representative video is given in Fig. 15. Formation of gas pockets is demonstrated by the video in Fig. 16.

Even though strongly nonlinear free-surface phenomena are observed for the larger forcing amplitude $\eta_{2a}/l = 0.03$ in

our experimental model tests done with $h/l = 0.35$, we attempted to compare our quasi-linear prediction and the corresponding experimental measurements of the steady-state maximum wave elevations at the walls. Results are reported in Figs. 17–19.

The measured signal was not exactly steady-state for several of the tested forcing frequencies. For the early-reported experimental results, standard deviations of the maximum wave elevation in the experimental steady-state condition were comparable with 1 mm, i.e., with the measurement error, but the experimental data for $\eta_{2a}/l = 0.03$ with $h/l = 0.35$ demonstrated standard deviations comparable with the forcing amplitude. The η_{2a}-scaled standard deviations of the measured signal are presented in Figs. 17–19 to identify the frequency ranges where they may matter. As it follows from the previous analysis for lower forcing amplitudes, the largest standard deviations are detected for σ between σ_2^* and σ_3^* where the free-surface nonlinearity is especially important. Just about these values of the forcing frequency, we observed most severe wave breaking. Furthermore, the change of the forcing amplitude for different forcing frequencies has been negligible for this experimental series, less than 1%, thus, we neglected it in our quasilinear modeling assuming $\eta_{2a}/l = 0.03$.
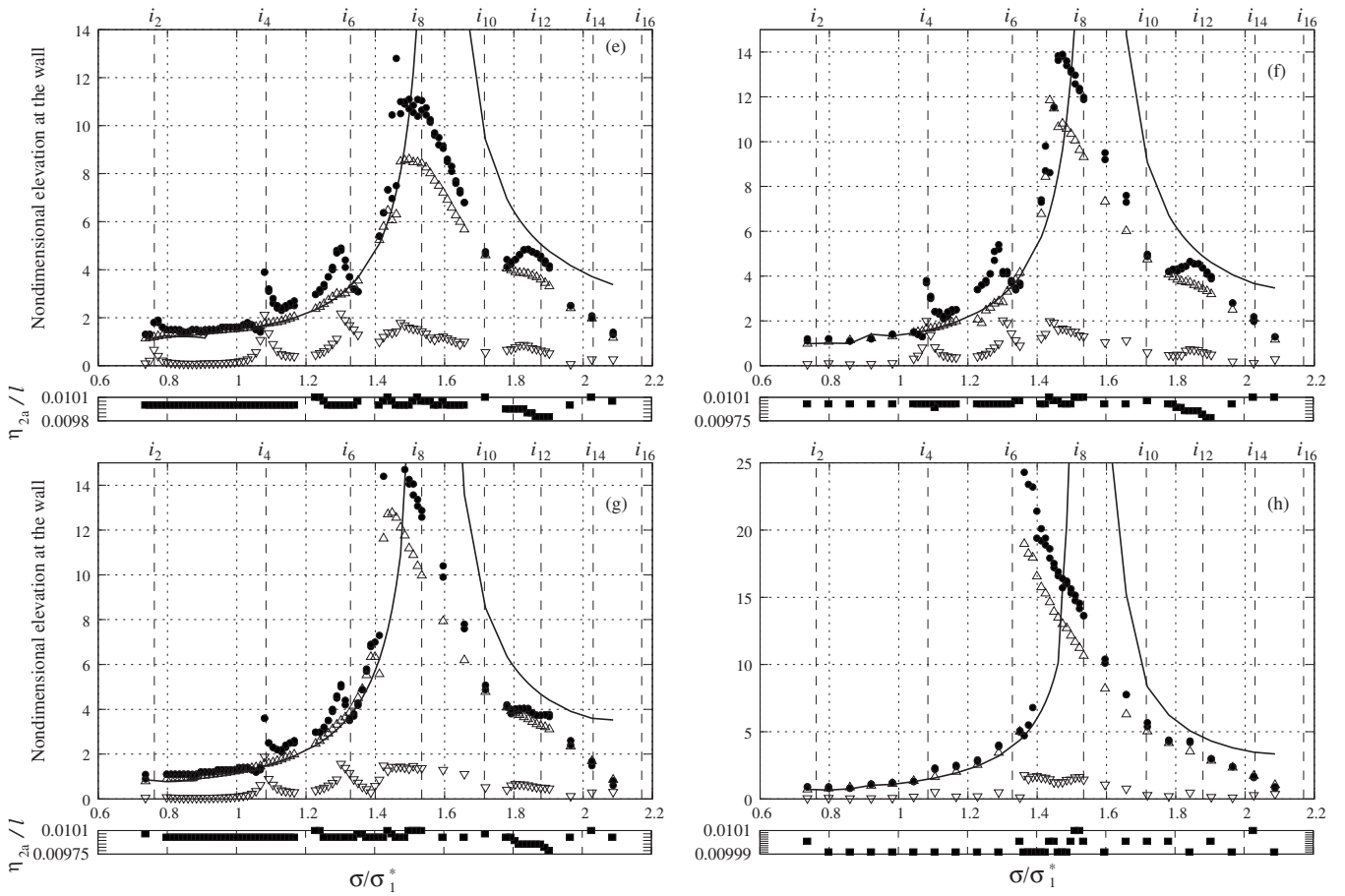
FIG. 14. The same as for the panels (e)–(h) in Fig. 6, but for the larger forcing amplitude $\eta_{2a}/l \approx 0.01$. Contribution of the first Fourier harmonics to the measured wave elevations (scaled by η_{2a}) is denoted by $\triangle$, but ∇ denotes contribution of the second Fourier harmonics. The values $\sigma/\sigma_1^* = i_{2k}, k \geq 1$ [see Eq. (34) and the corresponding vertical dashed lines] indicate the frequencies where the secondary resonance due to the second-order free-surface nonlinearity is expected.

We start our analysis with results in Fig. 17 which represents the case of the lower tested solidity ratios associated with the screens (a) and (b). The figure shows that the quasilinear theory does not satisfactorily quantify the free-surface elevations with increasing η_{2a}, but shows a correct trend in how resonance frequencies change. Furthermore, the case $\eta_{2a}/l = 0.03$ brings, from experimental point of view, several new physical phenomena. First of all, we note a
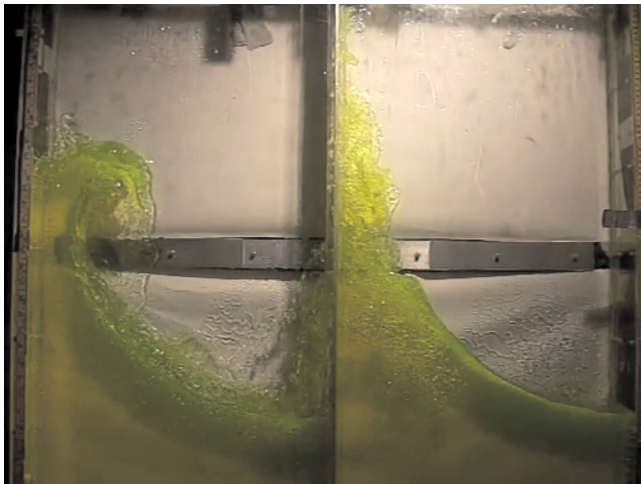

FIG. 15. (Color online) Representative video of the free-surface phenomena in experimental series with $\eta_{2a}/l = 0.03$ and $h/l = 0.35$. The video illustrates free-surface phenomena occurring for $\sigma/\sigma_1 = 1.328$ and Sn = 0.914 286 (enhanced online).[URL: http://dx.doi.org/10.1063/1.3562310.5]

FIG. 16. (Color online) Formation of a gas pocket at the vertical walls occurring for $\eta_{2a}/l = 0.03$ and $h/l = 0.35$. The photograph and video is given for $\sigma/\sigma_1 = 0.96$ and Sn = 0.472 857 (enhanced online).[URL: http://dx.doi.org/10.1063/1.3562310.6]
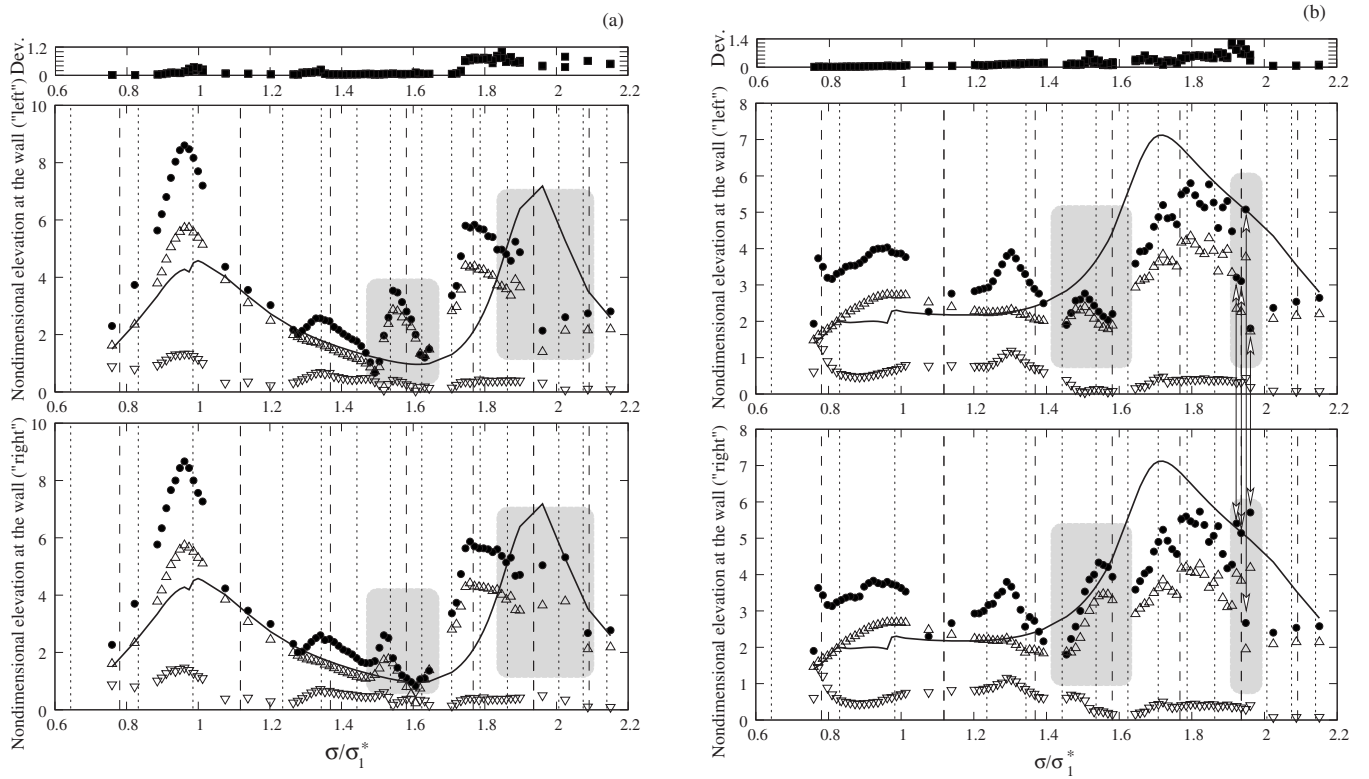
FIG. 17. The nondimensional experimental (●) and theoretical (solid line) maximum steady-state wave elevations at the "left" and "right" measurement probes (1 cm away from the wall) vs the forcing frequency; $h/l=0.35$ and $\eta_{2a}/l=0.03$. The wave elevations are scaled by the forcing amplitude η_{2a}, but the forcing frequency σ is scaled by the lowest natural sloshing frequency σ_1^* for the clean tank (3). "Dev." denotes the η_{2a}-scaled standard deviations of the measured maximum wave elevations in the experimental steady-state conditions. Contribution of the first Fourier harmonics to the measured wave elevations (scaled by η_{2a}) is denoted by $\triangle$, but $\triangledown$ denotes the η_{2a}-scaled contribution of the second Fourier harmonics. The dashed lines indicate the frequencies where the secondary resonance due to the second-order free-surface nonlinearity is expected by Eq. (34). The dotted lines show the frequencies where the secondary resonance due to the third-order free-surface nonlinearity is expected by Eq. (35). The shadow zones (with arrows) indicate two different experimental steady-state solutions occurring in Q_0^+ and Q_0^-. (a) Sn=0.472 857, $N=62, K=3.106$ 66, (b) Sn=0.687143, $N=37$, $K=15.8448$.

multibranching of the experimental response curves which appears as different experimentally detected steady-state wave elevations at the opposite measurement probes (henceforth, "left" and "right" probes). We mark this by shadow zones in Fig. 17. A hysteresis with the corresponding soft-spring type multibranching (see Fig. 3) is possible in the two limit cases, Sn=1 and 0. This hysteresis can, therefore, be expected in the left of $\sigma/\sigma_1^*=1$, 1.524, and 1.878. According to Faltinsen and Timokha,[12] a central slat-type screen with the tested solidity ratios in Fig. 17 can slightly shift this hysteresis to the left of aforementioned frequencies, but it cannot move it in the right direction along the horizontal axis. The multibranching phenomenon in the shadow zone occurs in other frequency ranges and, therefore, it cannot be related to the nonlinear sloshing phenomena known for clean rectangular tanks.

Furthermore, similar to the cases with $\eta_{2a}/l=0.01$ and $h/l=0.4$, we see many additional experimental resonance peaks. Earlier, these peaks were well clarified by the secondary resonance with amplification of the second Fourier harmonics. However, Fig. 17 shows that it is not the case for the larger forcing amplitude. A reason is that the position of the additional peaks is not clearly at $\sigma/\sigma_1^*\approx i_{2k}$ and the actual wave elevations cannot, generally, be approximated by the sum of the first and second harmonics contributions. Because

increasing forcing amplitude may lead to the secondary resonance by the third-order nonlinearity, we estimated the frequencies where this kind of the secondary resonance occurs. The corresponding condition $3\sigma\approx\sigma_{2k+1}$ gives

$$\frac{\sigma}{\sigma_1^*}\approx\frac{\sigma_{2k+1}}{3\sigma_1^*}=i_{2k+1},\quad k=1,2,\dots. \tag{35}$$

The values of i_{2k+1} are marked by the vertical dotted lines in Fig. 17. Summarizing the dotted and dashed lines gives a 'net' of possible secondary resonances (due to the second- and third-order free-surface nonlinearities) in the studied frequency range. A dedicated study is required to quantify the reason for the experimentally detected multibranching and additional resonance peaks.

Figure 18 demonstrates the theoretical and experimental results for the screens (c)–(f) with larger solidity ratios. The quasilinear theory shows a clear linear resonance at $\sigma/\sigma_1^*=1.6$, but the experiments indicate a more complicated response. The multiple-peak response structure continuously disappears from the panels (c)–(f) with increasing the solidity ratio so that the experimental case (f) shows a clear soft-spring type behavior at the primary resonance $\sigma/\sigma_1^*=1.6$ with an extra jump at $\sigma/\sigma_1^*\approx i_4$. Similar response curves were detected by the adaptive modal sloshing theory for a
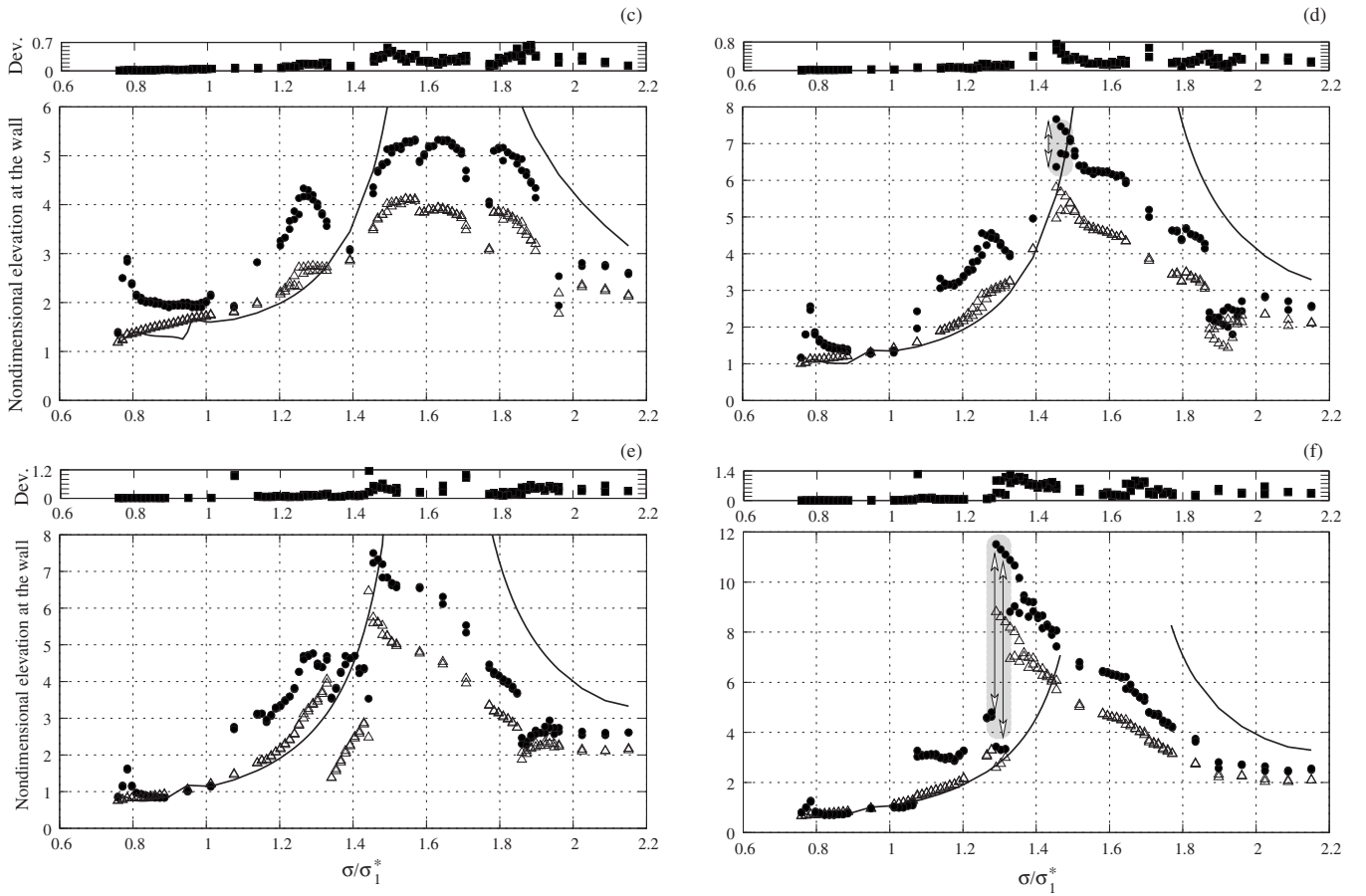
FIG. 18. The nondimensional experimental (●) and theoretical (solid line) maximum steady-state wave elevations at the 'left' and 'right' measurement probes (1 cm away from the wall) vs the forcing frequency; $h/l=0.35$ and $\eta_{2a}/l=0.03$. The wave elevations are scaled by the forcing amplitude η_{2a}, but the forcing frequency σ is scaled by the lowest natural sloshing frequency σ_1^* for the clean tank (3). Dev. denotes the η_{2a}-scaled standard deviations of the measured maximum wave elevations in the experimental steady-state conditions. The η_{2a}-scaled contribution of the first Fourier harmonics to the measured wave elevations is denoted by △. The shadow zones (with arrows) indicate different experimental steady-state elevations for opposite sides of the tank (for different measurement probes). (c) Sn=0.790, N=25, K=43.1960; (d) Sn=0.841 429, N=19, K=82.9828; (e) Sn=0.892 857, N=13, K=197.846; (f) Sn=0.914 286, N=10, K=319.727.
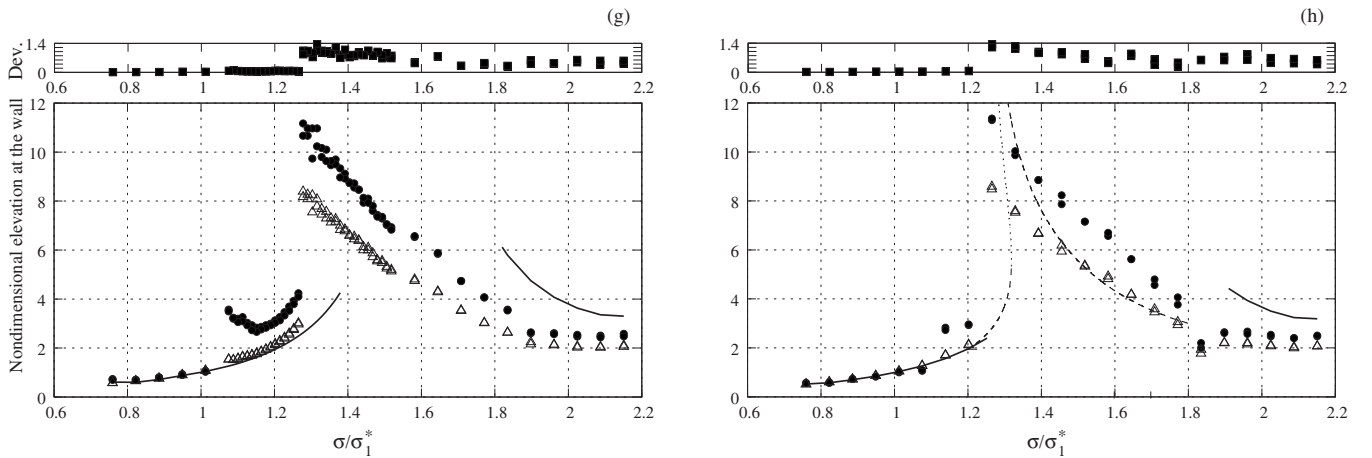

FIG. 19. The nondimensional experimental (●) and theoretical (solid line) maximum steady-state wave elevations at the measurement probes (1 cm away from the wall) vs the forcing frequency; $h/l=0.35$, $\eta_{2a}/l=0.03$. The wave elevations are scaled by the forcing amplitude η_{2a}, but the forcing frequency σ is scaled by the lowest natural sloshing frequency σ_1^* for the clean tank (3). Dev. denotes the η_{2a}-scaled standard deviations of the measured maximum wave elevations in the experimental steady-state conditions. The η_{2a}-scaled contribution of the first Fourier harmonics to the measured wave elevations is denoted by △. (g) Sn=0.935 714, N=8, K=587.348; (h) Sn=0.952 857, N=6, K=1120.55. The dashed line in (h) shows the first harmonics contribution by the single-dominant modal theory (Chap. 8 in Ref. 11) for Sn=1 (solid screen).

clean rectangular tank (see Sec. II). The trend continues in Fig. 19. This figure shows that the liquid sloshing dynamics becomes closer to that in the two compartments, Q_0^+ and Q_0^-, with a solid wall between them. One should remark that, starting with the case (f), the Runge–Kutta integration by the quasilinear modal theory becomes unstable in a neighborhood of the theoretical linear resonance $\sigma/\sigma_1^* \approx 1.6$.

V. CONCLUSIONS

Studies of resonant sloshing in a rectangular tank with screens are typically restricted to the screen solidity ratios $\mathrm{Sn} \lesssim 0.5$, the forcing frequencies close to the lowest natural frequency σ_1^* of the corresponding clean tank, and relatively small forcing amplitudes. For these input parameters, one can assume that the global liquid motions are close to those in the corresponding clean tank, and that the screen-induced flow separation (or a jet flow) plays the same role as a quadratic damping for linear oscillators (see a review on quadratic damping for linear oscillators in Ref. 15). Higher solidity ratios, $0.5 \lesssim \mathrm{Sn} \lesssim 0.95$, a limited number of the screen openings, $N \lesssim 50$, a wider range of the forcing frequencies, and increasing forcing amplitudes that are relevant for ship tanks with swash (perforated) bulkheads are studied in the present paper experimentally and theoretically.

New experimental model tests were performed for finite liquid depths, three forcing amplitudes $\eta_{2a}/l = 0.001$, 0.01, and 0.03, and eight different slat-type screens installed at the middle of a rectangular tank. The primary emphasis has been placed on the two-dimensional steady-state sloshing and the corresponding experimental wave elevation at the opposite tank walls (1 cm away from the wall). The forcing frequency interval covered the three lowest natural frequencies of the clean rectangular tank, σ_1^*, σ_2^*, and σ_3^*. In our measurements of the steady-state maximum elevations, a larger number of tests with small changes of the forcing frequency σ was performed in local ranges where the experiments detected a local (resonance) peak.

In our theoretical analysis, we assumed the global flow to be described by an inviscid incompressible liquid model with irrotational flow. The screen-induced flow separation (or jet flow) effect on the global flow was modeled by a pressure drop condition. The formula for the empirical pressure drop coefficient was taken from the literature. This condition should be true not only for a porous media, but also, e.g., for orifice meter device with a single hole. The letter fact is important for higher solidity ratios of the experimental screens leading to a limit number of slots below the free surface. It is a matter of comparison with model test of, for instance, wave elevation that the empirical pressure drop condition makes sense. Our results for small excitation amplitude documented this fact. The multimodal method with linearized free-surface conditions was employed, i.e., we included into our theoretical model the screen-induced effect on the global flow, but neglected the free-surface nonlinearity.

Comparing the experimental and theoretical results for the three tested forcing amplitudes made it possible to estimate the effect of the free-surface nonlinearity. It is almost negligible for the lowest forcing amplitude $\eta_{2a}/l = 0.001$ with $0.5 \lesssim \mathrm{Sn} \lesssim 0.95$. Noticeable discrepancies between theory and experiments due to the free-surface nonlinearity are only established for the limit tested values, $\mathrm{Sn} = 0.4725$ and 0.951 25. An important conclusion for this forcing amplitude is that the larger amplitude response is found not at the primary resonance of the corresponding clean tank, σ_1^*, but rather at the natural frequency responsible for the second antisymmetric mode. According to Ref. 12, the natural sloshing frequency σ_3 for the screen-equipped rectangular tank monotonically decreases from σ_3^* to σ_2^* as Sn increases from 0.5 to 1. The reason is that the resonant excitations with σ away from σ_1^* cause a lower cross-flow through the screen. It is therefore understandable, that we should expect most severe nonlinear sloshing effects around σ_3 when η_{2a}/l increases. Experimental measurements and visual observations confirm this fact. Wave breaking, runups, transition to three-dimensional motions, and other specific free-surface phenomena were found just in a frequency range around σ_3. Photographs and videos are presented to illustrate them.

Analyzing the results for $\eta_{2a}/l = 0.01$ made it possible to understand that the free-surface nonlinearity causes sufficient energy content to symmetric modes due to the secondary resonance. This is a novelty for the screen-equipped tanks relative to the corresponding clean tanks for which amplification of higher modes due to the secondary resonance requires, normally, larger forcing amplitude. A possible reason is that the symmetric modes do not lead to a cross-flow through the screen and, therefore, are almost undamped, in contrast to the antisymmetric ones. This implies that the same-order forcing of symmetric and antisymmetric modes should give a larger response of the symmetric modes. In order to describe the associated nonlinear sloshing, we should, in the future, employ the *adaptive nonlinear* multimodal method.[5,22]

Multibranch experimental response curves are detected for $\eta_{2a}/l = 0.03$ in certain frequency ranges in a neighborhood of σ_2^* and σ_3^* where we cannot expect the soft-spring type behavior associated with nonlinear sloshing in a clean rectangular tank. Our quasilinear theory is not able to explain it. An explanation may come from analyzing possible secondary resonances due to the second- and third-order free-surface nonlinearities. Indeed, a few possibilities for the secondary resonance are detected at σ_1^* and, as a consequence, the quasilinear theory qualitatively well describes the main harmonics contribution of the actual wave elevations when $\sigma \approx \sigma_1^*$. However, there exist numerous possibilities for the secondary resonance in a frequency range covering σ_2^* and σ_3^* where the experiments detect the most severe free-surface phenomena and the multibranching occurs.

APPENDIX A: RELATIONS IN EQS. (25) AND (26)

Remembering that the natural sloshing modes φ_i satisfy the Laplace equation and the zero-Neumann condition on the wetted tank surface, inserting Eq. (24) into the time-independent relations Eqs. (5a)–(5c) gives

$$\nabla^2 p_2 = 0 \quad \text{in} \quad Q_0^{\pm}, \quad \frac{\partial p_2}{\partial n} = 0 \quad \text{on} \quad S_{0b}^{\pm} \cup S_{0w}^{\pm} \qquad \text{(A1)}$$

for integrand p_2 in the modified velocity potential Eq. (24).

Inserting the modal solutions Eqs. (7) and (24) into the kinematic boundary condition Eq. (5d) and remembering that

$$\frac{\partial \varphi_i}{\partial z}(y,0) = \kappa_i \varphi_i(y,0) = \kappa_i f_i(y) \qquad \text{(A2)}$$

due to the corresponding boundary condition on $\Sigma_0^{\pm}$ in the spectral problem Eq. (9) leads to the relation

$$\frac{1}{\rho} \int_{t_0}^{t} \frac{\partial p_2}{\partial z}(y,0,t_1) dt_1 = 0 \qquad \text{(A3)}$$

to be fulfilled for any instant t. The latter means that the integrand $\left(\frac{\partial p_2}{\partial z}\right)(y,0,t)$ should be zero, and we arrive at the zero-Neumann boundary condition Eq. (25a) which is further used in the boundary value problem Eq. (26).

Finally, inserting the modal solution Eqs. (7) and (24) into the dynamic boundary condition Eq. (5e) with relation Eq. (A2) gives the boundary condition Eq. (25b).

[1] J. Love and M. Tait, "Nonlinear simulation of a tuned liquid damper with damping screens using a modal expansion technique," J. Fluids Struct. **26**, 1058 (2010).

[2] S. Kaneko and M. Ishikawa, "Modelling of tuned liquid damper with submerged nets," ASME J. Pressure Vessel Technol. **121**, 334 (1999).

[3] M. Tait, A. El Damatty, N. Isyumov, and M. Siddique, "Numerical flow models to simulate tuned liquid dampers (TLD) with slat screens," J. Fluids Struct. **20**, 1007 (2005).

[4] P. Warnitchai and T. Pinkaew, "Modelling of liquid sloshing in rectangular tanks with flow-dampening devices," Eng. Struct. **20**, 593 (1998).

[5] O. M. Faltinsen and A. N. Timokha, "Adaptive multimodal approach to nonlinear sloshing in a rectangular tank," J. Fluid Mech. **432**, 167 (2001).

[6] R. D. Blevins, *Applied Fluid Dynamics* (Krieger Publishing Company, Malabar, FL, 1992).

[7] E. M. Laws and J. L. Livesey, "Flow through screens," Annu. Rev. Fluid Mech. **10**, 247 (1978).

[8] B. Molin, "On the added mass and damping of periodic arrays of fully or partially porous disks," J. Fluids Struct. **15**, 275 (2001).

[9] O. M. Faltinsen, R. Firoozkoohi, and A. N. Timokha, "Analytical modeling of liquid sloshing in a two-dimensional rectangular tank with a slat screen," J. Eng. Math. (in press).

[10] H. N. Abramson, "The dynamic behavior of liquids in a moving container," Technical Report SP-106, NASA, Washington, D.C., 1966.

[11] O. M. Faltinsen and A. N. Timokha, *Sloshing* (Cambridge University Press, Cambridge, 2009).

[12] O. M. Faltinsen and A. N. Timokha, "Natural sloshing frequencies and modes in a rectangular tank with a slat-type screen," J. Sound Vib. **330**, 1490 (2011).

[13] R. Porter and D. Evans, "Complementary approximations to wave scattering by vertical barriers," J. Fluid Mech. **294**, 155 (1995).

[14] D. Evans and P. McIver, "Resonant frequencies in a container with vertical baffles," J. Fluid Mech. **175**, 295 (1987).

[15] L. Cveticanin, "Oscillator with strong quadratic damping force," Publications de l'Institut Mathèmatique **85**, 119 (2009).

[16] M. Eastham, "An eigenvalue problem with parameter in the boundary condition," Q. J. Math. **13**, 304 (1962).

[17] S. F. Feschenko, I. A. Lukovsky, B. I. Rabinovich, and L. V. Dokuchaev, *Methods for Determining Added Fluid Mass in Mobile Cavities* (Naukova Dumka, Kiev, 1969) (in Russian).

[18] J. Morand and R. Ohayon, *Fluid structure interaction. Applied numerical methods* (Wiley, New York, 1995).

[19] W. D. Baines and E. G. Peterson, "An investigation of flow through screens," Trans. ASME **73**, 467 (1951).

[20] J. Weisbach, *Die Experimental-Hydraulik* (Engelehardt, Freiburg, 1855).

[21] O. Faltinsen, O. Rognebakke, and A. Timokha, "Resonant three-dimensional nonlinear sloshing in a square base basin," J. Fluid Mech. **487**, 1 (2003).

[22] O. Faltinsen, O. Rognebakke, and A. Timokha, "Transient and steady-state amplitudes of resonant three-dimensional sloshing in a square base tank with a finite fluid depth," Phys. Fluids **18**, 012103 (2006).